Pt-free silver nanoalloy electrocatalysts for oxygen reduction reaction in alkaline media

Qaseem, Adnan; Chen, Fuyi; Wu, Xiaoqiang; Johnston, Roy L.

DOI:
10.1039/c5cy02270c

Document Version
Peer reviewed version

Citation for published version (Harvard):
Qaseem, A, Chen, F, Wu, X & Johnston, RL 2016, 'Pt-free silver nanoalloy electrocatalysts for oxygen reduction reaction in alkaline media', *Catalysis Science and Technology*, vol. 6, no. 10, pp. 3317-3340. https://doi.org/10.1039/c5cy02270c

Catalysis Science & Technology

Accepted Manuscript

This article can be cited before page numbers have been issued, to do this please use: A. Qaseem, F. Chen, X. Wu and R. L. Johnston, *Catal. Sci. Technol.*, 2016, DOI: 10.1039/C5CY02270C.

ROYAL SOCIETY OF CHEMISTRY

www.rsc.org/catalysis

View Article Online
DOI: 10.1039/C5CY02270C

Pt-free Silver Nanoalloy Electrocatalysts for Oxygen Reduction Reaction in Alkaline Media

Adnan Qaseem [a], Fuyi Chen*[,a], Xiaoqiang Wu [a] and Roy L. Johnston*[,b]

[a] State Key Laboratory of Solidification Processing, Northwestern Polytechnical University, Xian, 710072, China

[b] Department of Chemistry, University of Birmingham, Birmingham, B15 2TT, U.K.

*Corresponding author. fuyichen@nwpu.edu.cn (Fuyi Chen). r.l.johnston@bham.ac.uk (Roy L. Johnston)

Abstract:

Oxygen reduction reaction (ORR) plays a crucial role in electrochemical energy conversion and storage devices such as alkaline fuel cells and metal-air batteries. These systems which could employ non platinum catalysts for oxygen reduction are cheaper and stable alternatives to their expensive counterparts like proton exchange membrane fuel cells (PEMFC) working on platinum based catalysts. Various binary and ternary silver nanoalloys have been reported to act as efficient electrocatalysts for ORR in alkaline fuel cells and batteries. Herein, we present a critical review on the recent advances made in silver nanoalloy electrocatalysts for ORR in alkaline media. The mechanism of ORR on nanoalloys is described; the effect of structure and composition of various silver nanoalloys (including Ag-Cu, Ag-Pd, Ag-Au, Ag-Co etc.) on their ORR activity and stability is discussed. The rational design of electrocatalysts in order to maximize the catalytically active sites on the surface of the electrocatalysts for oxygen reduction reaction is also reviewed. Finally, we provide insights into the remaining challenges and directions for future perspectives and research.

Keywords

Metal-Air Batteries, Alkaline Fuel Cells, Oxygen Reduction Reaction, Silver Nanoalloys, Electrocatalyst

View Article Online
DOI: 10.1039/C5CY02270C

1 Introduction.

World has seen industrialization at an enormous pace in the past century. This accompanied with the tremendous growth of human population has escalated the energy demand at unprecedented levels. The traditional approach of burning fossil fuels to meet this thirst for energy has its own implications on the environment.[1, 2] Growing environmental concerns along with the declining fossil fuel reserves have provided the impetus to look for renewable sources of energy which are widely available and sustainable. [3, 4]

High energy density metal-air batteries and fuel cells are advanced energy storage and conversion systems to meet the requirement of environmentally sustainable energy sources.[5-8] Metal-air battery systems which have high energy like the Li-air battery is equivalent to gasoline in terms of practical energy density. The practical energy density from a gasoline engine with 12.5% conversion is 1700 Wh/Kg. In alkaline electrolytes theoretical specific energies for Li-air battery is reported to be 2,353 Wh/kg in the charged state and 1,905 Wh/kg in the discharged state.[9] Also the alkaline Zn-air battery has a theoretical energy density of more than three times than the widely used Li-ion battery. The specific details for some popular batteries are tabulated in Table 1. However the commercialization of metal-air battery is largely impeded by the sluggish ORR at the cathode side along with stability and cost of these systems. Similarly the commercialization of alkaline fuel cells (AFCs) remains at large because of the safety issues, CO_2 sensitivity of electrolyte along with the exorbitant cost of Pt catalyst for the cathodic ORR.[10, 11] It is with the recent advancements in the field of nanocatalysts and anion exchange membranes that the anion exchange membrane fuel cells (AEMFCs) have reemerged as a possible alternate to PEMFCs.[12-14] The high cost and limited reserves of Pt metal is a major issue impeding commercialization of fuel cell technology for widespread use. The U.S. department of energy (DOE) has set a target price of 40 USD/KW for a model 80 KW fuel cell system by 2020. Nearly half of the cost of PEMFC stack arises from the Pt based electrocatalyst with long term stability still short of the DOE target of 40,000 hrs for stationary and 5000 hrs for mobile applications. [15, 16]

Unlike the PEMFC that employ expensive platinum based catalysts for ORR at the cathode end of the cell, the alkaline fuel cells and alkaline metal-air battery systems offer the advantage of use of inexpensive Pt-free electrocatalysts for ORR. The stability of the metallic catalyst systems in terms of potential and pH is described by the pourbaix diagram. [17] The highly corrosive acidic conditions in low pH systems make the use of costly platinum group metals and alloys mandatory for the long term stability of PEMFC. Increasing the pH broadens the spectrum of metallic systems by allowing the use of non-platinum materials as catalysts for ORR. The most significant advantage of ORR under alkaline conditions are the faster kinetics and lower overpotentials, potentially allowing use of inexpensive, platinum free metal catalysts such as silver and its alloys, doped carbons , transition metal oxides including spinels and perovskites and transition metal macromolecules like metal phthalocyanines for the reduction reaction at the cathode. [18-23] The shift of pH from 0 to 14 improves the ORR kinetics by decreasing the adsorption strength of anion species. [24] Surface independent electron transfers processes are active in alkaline media resulting in the more facile kinetics of ORR. [25] Silver and its alloys are much more stable and highly active for ORR in the alkaline conditions. The price of silver being more than 50 times less than platinum makes it an attractive low cost alternative. Improvement of the electrocatalytic activity of silver by nanoalloying has been of great significance for the realization of economically viable metal-air batteries and alkaline fuel cells.

View Article Online
DOI: 10.1039/C5CY02270C

Table 1 Battery Comparison

Battery Type	Theoretical specific Energy (Wh/Kg)	Practical Specific Energy. (Wh/Kg)	Charge Capacity (mAh/g)	Equilibrium Cell Potential (V)	Chemical Reaction
Li-Air	11431	1500	3842	2.96	$2Li+O_2 \rightarrow Li_2O_2$
Li-OH	2200	600	639	3.45	$4Li + 6H_2O + O_2 \rightarrow 4(LiOH.H_2O)$
Zn-Air	1353	400	815	1.65	$2Zn + O_2 \rightarrow 2ZnO$
Al-air	8140	350	2965	2.71	$4Al + 3O_2 + 6H_2O \rightarrow Al(OH)_3$
Mg-air	6800	700	2200	3.09	$2Mg + O_2 + 2H_2O \rightarrow 2Mg(OH)_2$
Ni-Cd	245	60	200	1.2	$2NiO(OH)+Cd+2H_2O \rightarrow 2Ni(OH)_2+Cd(OH)_2$
Ni-MH	280	90	160	1.2	$xNi(OH)_2+M \rightarrow xNiOOH+MH_x$
Li-ion	400	135	273	3.6	$LiCoO_2+C \rightarrow Li_xC+Li_{1-x}CoO_2$
Pb-Acid	170	40	83	2.1	$Pb + PbO_2+2H_2SO_4 \rightarrow 2PbSO_4+2 H_2O$

In order to improve activity and stability, various binary and ternary silver nanoalloys have been proposed as one of the efficient electrocatalysts for ORR in alkaline fuel cells and batteries. Nanoalloys are nanoscale (upto 100 nm in size) alloys of two or more metals. These nanocatalysts have the advantage of extremely high surface area due to tiny particle size accompanied with the possibility of synergistic effects from the constituent elements. [26-28] A wide variety of compositions and atomistic arrangements are possible including core-shell, multilayer, janus, thin films, amorphous and ordered-disordered nanoalloy systems (Figure 1). [29-31] The rational design of these nanocatalysts based on a combination of first principle simulations and experimental techniques has played an important role in developing highly active Pt-based and Pt-free catalysts for ORR in fuel cells and metal–air batteries. The computational knowledge has enabled a better understanding of the mechanism of ORR in energy conversion and storage processes. Based on the calculations on different adsorbates i.e. reaction intermediates on a catalyst surface, rate limiting steps for catalysts have been identified. [32-34] Elements such as Ag and Cu which are weak ORR catalysts individually have been found to be active toward ORR in alkaline conditions when alloyed at nanoscale. [35, 36] Ag has a weak binding for ORR intermediates while Cu has a too strong binding for ORR intermediate such as O, OH and OOH. [32, 34, 37] Nanoalloying of the Ag-Cu promotes the binding of the ORR intermediates to an optimum level which promotes the Ag-Cu nanoalloy catalytic activity. Another striking example is of Ag skin on Au core. [38] Gold is a poor ORR catalyst like Ag for ORR due to it weak binding of ORR intermediates but a monolayer of Ag on Au has been identified by DFT calculations as an active alloy for ORR. This promotion is attributed to the enhanced surface reactivity of Ag skin on Au core nanocatalyst. In the recent years a number of innovative structures and compositions have been identified as candidate catalysts for ORR. [39-42] Significant progress in comprehension of the reaction mechanisms during the ORR on the surface of nanoalloy catalysts and understanding of how the thermodynamics and kinetics of ORR are affected by the alloying of elements at the nanoscale has been achieved by the computational assisted experimental research in recent years. [43-45]

This review encompasses the recent advances in the field of Pt-free silver nanoalloy catalysts for ORR in alkaline media. We will briefly describe the mechanism of ORR in alkaline media along with the identification of reaction pathways on the surface of the nanocatalyst. This will be followed by a detailed discussion on the silver based nanoalloy catalysts. The effect of composition and structure of the nanocatalyst on its activity and stability during ORR will be reviewed. Moreover, different mechanisms such as ligand, geometric and ensemble effect, playing role in these nanoalloys will be also described. Finally the review will concluded with possible directions for future research work in the field of Pt-free nanoalloy catalyst for ORR in the alkaline media.

View Article Online
DOI: 10.1039/C5CY02270C

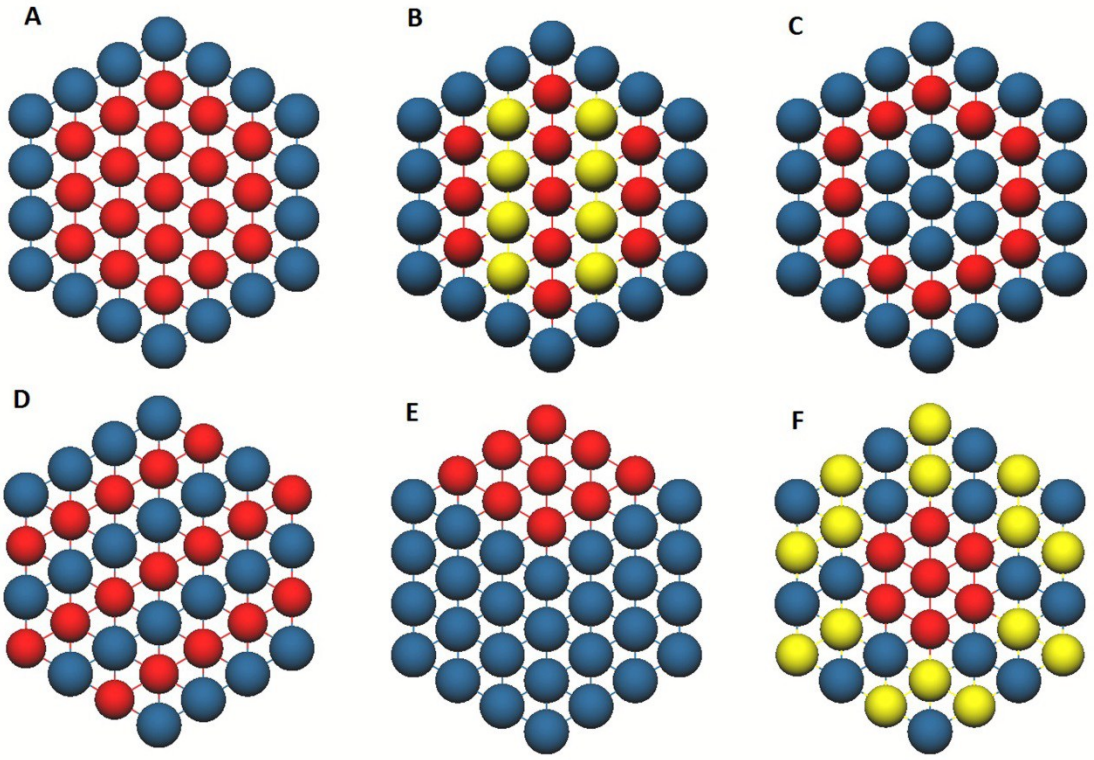

Figure 1 Schematic of atomistic arrangements of nanoalloys, (A) monolayer on pure metal, (B) monolayer on solid solution, (C) subsurface monolayer, (D) ordered intermetallic, (E) Janus and (F) alloy shell.

2 ORR mechanism in alkaline media.

Electrocatalytic reduction of oxygen in alkaline electrolytes involves the transfer of 4 electrons to molecular oxygen resulting in the formation of 4 hydroxyls as stated in equation 1 for pH 14.

$$O_2 + 4e^- + 2H_2O \rightleftarrows 4OH^- \; ; \; E^o = 1.227 \text{ V vs. RHE} \quad (1)$$

Transfer of 2 electrons can result in incomplete reduction accompanied with the formation of peroxide:

$$O_2 + 2e^- + H_2O \rightleftarrows HO_2^- + OH^- \; ; \; E^o = 0.75 \text{ V vs. RHE} \quad (2)$$

This can further be reduced by addition of 2 more electrons as:

$$HO_2^- + 2e^- + H_2O \rightleftarrows 3OH^- \; ; \; E^o = 1.704 \text{ V vs. RHE} \quad (3)$$

Or by disproportionation as:

$$2HO_2^- \rightleftarrows 2OH^- + O_2 \quad (4)$$

The ORR is a multistep reaction involving the formation of intermediates such as O^{2-}, O, OH^-, HO_2^-, and OOH. [46-48] ORR is affected by the formation and stability of these intermediates on the surface of the catalyst which in turn regulate the activity of the catalyst. [32, 34, 49, 50] ORR accompanied by the formation of peroxide is undesirable and limits the efficiency of the catalyst. It is highly desirable that the reduction takes place with the complete transfer of 4 electrons to the oxygen molecule. Owing to the limited solubility of oxygen in aqueous solutions i.e. ~ 1.26 x 10-3 mol/L, techniques based on convective transport of reactants in the solution such as the Rotating Disk Electrode (RDE) and Rotating Ring Disk Electrode (RRDE) are employed to identify the electron transfer mechanism and the associated formation of intermediates. [51-55] The selectivity of $4e^-$ or $2e^-$ pathway is estimated via Koutecky Levich equation.

$$\frac{1}{j} = \frac{1}{j_K} + \frac{1}{j_d} \quad (5)$$

View Article Online
DOI: 10.1039/C5CY02270C

Where j_k is the kinetic current density and j_d is the diffusion limiting current density.
Also,

$$j_k = nFkC_o \quad (6a)$$

And

$$j_d = 0.62\, nFC_o D_o^{2/3} v^{-1/6} \omega^{1/2} \quad (6b)$$

Here ω is the angular velocity, n is transferred electron number, F is the Faraday constant, C_o is the bulk concentration of O_2, D_o is the diffusion coefficient of O_2 in electrolyte, v is the kinematic viscosity of the electrolyte, and k is the electron-transfer rate constant. Fraction of peroxide formation is recorded by the ring electrode of the RRDE and accompanied electron transfer number is calculated as:

$$X_{HO_2^-} = \frac{2I_R/N}{I_D + I_R/N} \quad (7)$$

$$n_e = \frac{4I_D}{I_D + I_R/N} \quad (8)$$

Where I_D is the disk current, I_R is the ring current, and N is the collection efficiency. As it is not possible to distinguish the current due to direct 4 electron transfer and by series 4 electron transfer in RRDE, it is quite common that the term pseudo-4 electron pathway is used by the researchers. The mechanism of ORR has been investigated on Pt and its alloys by X-ray absorption and spectroscopic studies. Previous works by Damjanovic and others report that the rate determining step for metals like Pt and Ag is the 1st electron transfer with or without protonation. [56-58]

$$O_{2,a} + e^- \rightarrow O_2^- \; ; \; E^o = 0.526 \pm 0.856 \text{ V vs. RHE} \quad (9)$$

The potential for this reaction does not change in changing pH from 0 to 13 on Ag(111) surface. [56, 59, 60] This pH independence causes a decrease in overpotential η for reaction (9) from 1.53 V at pH 0 to 0.7 V at pH 14. [25, 61] The decrease of η with pH is one the main reasons permitting the use of a variety of Pt-free catalysts for ORR in alkaline media. Following the first electron transfer, ORR can take place by direct OH^- formation or by HO_2^- intermediate. The kinetics of ORR is revealed by the Tafel plot of ORR on catalyst surface. Two distinctive regions are observed on the basis of overpotential on Pt. In the low over potential regime marked with a Tafel slope of -60 mV/dec there is a pH dependence of -30 mV/pH unit whereas the high overpotential region has a Tafel slope of -120 mV/dec with no dependence on pH. [62-65] The Tafel slope of -2.3RT/F (-60 mV/dec) obtained in the low overpotential region follows the Temkin adsorption isotherm because of the intermediate oxide coverage arising from ORR reaction intermediates. In the high overpotential region marked with the Tafel slope of -2 x 2.3RT/F (-120 mV/dec), adsorption is governed by the Langmuir isotherm as significant oxide coverage ceases to exist at these potentials. [66-68] The adsorbed OH species on Pt surfaces that impede O_2 adsorption arise mostly from water activation whereas the ORR reaction intermediates typically exhibit lower coverage values compared to water activation products. [69] In the entire pH range and current density region the reaction order with respect to molecular O_2 is unity. These observations, along with the first-order dependence on O_2 partial pressure, are in agreement with the proposed first electron transfer to adsorbed O_2 to form superoxide anion as the rate-limiting step. [22, 57, 62, 65, 66, 68] A detailed reaction scheme on Pt-metal surfaces involving the formation of both Peroxide and OH is proposed by Azdic *et al.* for alkaline electrolytes. [70] Like Pt, ORR on Ag surface in alkaline medium takes place with pseudo $4e^-$ transfer. Reaction order is one and the Tafel plots are also marked with great similarity with 2 distinct slope regions (Figure 2). [20, 56, 61, 71-75] Experimental data supports the notion of similar reaction mechanism to that of Pt. However, unlike Pt which shows strong pH dependence at low overpotential, ORR on Ag shows no dependence on the pH. Based on this nonconformance, Sepa *et al.* suggested a different mechanism in which the rate-limiting step is a chemical step after the 1st electron transfer for the low overpotential but the same step as Pt, i.e. 1st electron transfer for the high overpotential. [56] An alternate view was put forward by Yeager *et al.* who suggested that oxygen reduction on Pt surfaces involves dissociative chemisorption of oxygen molecule including the initial adsorption of O_2 with or without an electron transfer as the rate determining step. [76] In gas phase studies there are several evidence of

View Article Online
DOI: 10.1039/C5CY02270C

dissociative chemisorption of molecular O_2. On the other hand in electrochemical conditions where solvation effects and adsorbed species are present, adsorption of molecular O_2 is likely to be weakened.

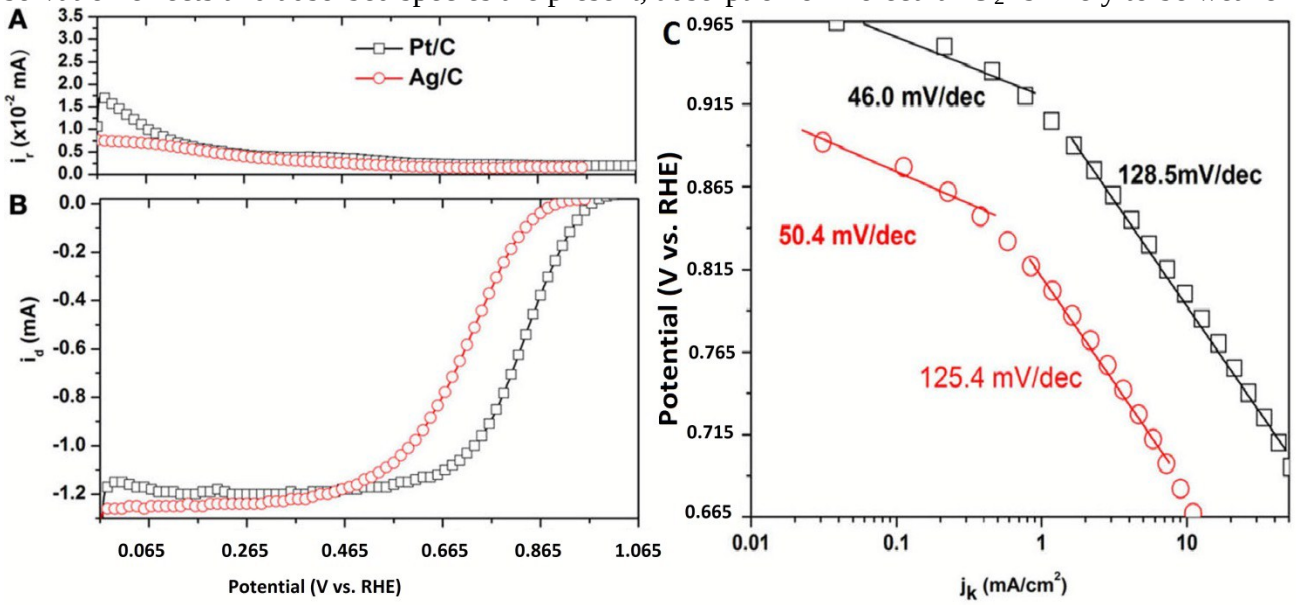

Figure 2 Linear sweep voltammograms of Pt/C and Ag/C catalysts for the oxygen reduction reaction in O_2-saturated 0.1M KOH. Scan rate: 10mV/s; rotation rate: 2500rpm; collection efficiency: 0.23; room temperature. (A) Ring current; (B) Steady state polarization curves; (C) Tafel plots. Adapted with permission from ref. 20.

2.1 Facet Effect

Blizanac *et al.* investigated the structural sensitivity of silver towards ORR by using RRDE. [71] The activity towards ORR increases in the order (110)>(111)>(100) at the same temperature and overpotential. Activation energies for the ORR on each of these facets were estimated at three different overpotential from three different temperatures using the Arrhenius plots. At all the overpotentials the activation energy for ORR was found to be maximum for (100) plane and minimum for the (110) plane. The different activity of these surfaces can be explained in terms of a balance between the adsorption strengths of OH and O_2 on these facets. Ag(110) has the highest attraction for OH, and should therefore show suppressed ORR activity due to higher OH coverage but also because of the relatively high affinity of Ag(110) for O_2 it leads to a higher ORR activity. On the other hand the effects of the lower affinities of OH and O_2 for adsorption on Ag(100) was established to result in lower ORR activity on this surface. The observation that the facet with the highest affinity for OH has the highest ORR activity may be explained by noting that the surface OH coverage remains fairly low as compared with the OH coverage on Pt on all three Ag surfaces. The major difference in OH adsorption on Ag(hkl) and Pt(hkl) surfaces is that whereas the OH adsorbed layer on Ag(hkl) is reversible, on Pt(hkl) the reversible adsorption is followed by an irreversible adsorption of OH. [77] As a result of this reversible/irreversible transition the hysteresis found in Pt(hkl) in the current between the anodic and cathodic sweeps is not observed on Ag(hkl). The reversible voltammetric features as well as the lack of hysteresis in the ORR currents on Ag(hkl) manifests the weaker adsorption of OH on Ag as compared to Pt. The affinity of Ag for oxygen was found to be good enough to break the O-O bond and lead to four-electron oxygen reduction reaction.

Silver nanodecahedra and nanocubes were explored for the effect of facet on ORR by using a combination of computational and experimental approach by Wang *et al.* [78] Nanodecahedra were surrounded by ten Ag (111) facets, while nanocubes were surrounded by six Ag (100) facets. Koutecky Levich plots revealed the electron transfer number of 3.8 for the nanodecahedra while 3.1 and 3.7 for nanocubes. 4 electron transfer for ORR on decahedra was proposed while the 2 electron path was

View Article Online
DOI: 10.1039/C5CY02270C

dominant for the nanocubes with the (100) facet. This difference of activity was attributed to the different adsorption behavior of OH* intermediate on the two type of facets. Using DFT it was found that higher adsorption energy of OH* on Ag(100) lead to fewer available sites for the O_2 and OOH* which hindered the ORR kinetics.

2.2 pH Effect

The effect of pH on the ORR mechanism was investigated on Ag(111) by performing RRDE in 0.1 M KOH and 0.1 M $HClO_4$. [61] In acidic environment 2 electron mechanism was dominant at lower overpotential followed by a combined $2e^-$ and $4e^-$ at higher overpotential. The changes of acidic to alkaline media lower the overpotential by 400 mV. ORR Proceed by 4 electron transfer with negligible peroxide production. The Tafel plot in alkaline electrolyte revealed 2 distinct regions marked with slope of -85 mV/dec at low overpotential and other with a slope of -125 mV/dec at higher overpotential. This supports the notion of a similar reaction mechanism to Pt for the silver surface in alkaline condition. However on Pt surface 4 electron transfer path was dominant in both strong alkali and acid. [22, 65, 79, 80]

2.3 Outer Helmholtz Plane Effect

Mukerjee *et al.* have proposed the outer sphere electron transfer mechanism to be dominant for non-noble metals in alkaline media. [81] The origin of this proposition lies in the change of the double layer structure at electrode electrolyte interface with the increase of pH (Figure 3). The decrease of overpotential for the first electron transfer as in Equation (9) implies that the strong chemisorption of O_2 is not necessary and long range dipole-dipole interaction could be sufficient to overcome the potential for this reaction. The electron transfer takes place by the interaction of adsorbed OH in the inner sphere at the electrode surface and the hydrated oxygen i.e. $O_2.nH_2O$ in the outer sphere.

This interaction is also present in acids but the barrier for the electron transfer is high enough to prevent the transfer through this mechanism. In alkaline media however this interaction leads to formation of HO_2^- which desorbs into the electrolyte. The reaction steps for the adsorbed OH at metal with solvated molecular oxygen cluster are described by equations (10-14) :

$$M\cdots OH + [O_2.nH_2O]_{aq} + e^- \rightarrow M\cdots OH + [O_2^{o,-}.nH_2O]_{aq} \quad (10)$$

$$[O_2^{o,-}.nH_2O]_{aq} \rightarrow (O_2^{o,-})_{ads} + nH_2O \quad (11)$$

$$(O_2^{o,-})_{ads} + H_2O \rightarrow (HO_2^o)_{ads} + OH^- \quad (12)$$

$$(HO_2^o)_{ads} + e^- \rightarrow (HO_2^-)_{ads} \quad (13)$$

$$(HO_2^-)_{ads} \rightarrow (HO_2^-)_{aq} \quad (14)$$

The surface independent nature of M-OH interaction with solvated O_2 in the Outer Helmholtz Plane (OHP) leads to the availability of variety of metals for ORR in alkaline media. On noble metal such as Pt both inner Helmholtz Plane (IHP) and OHP mechanisms are likely to occur depending upon the oxide coverage. Molecular dynamics simulations have confirmed the effect of adsorbed OH^- in impeding the ORR kinetics. [82] Pt(100) surface was calculated to have the maximum density of hydrogen bonding and the most compact bonding network. A potential barrier for O_2 migration was found between the first and second adsorption layers on the potential of mean force (PMF) curves on all three low index surfaces. The potential barriers on the (111) and (100) surfaces were 2.6 and 3.4 kcal/mol in water and 2.9 and 3.8 kcal/mol in alkaline media. A higher number of hydrogen bonds were generated by OH^- ions and H_2O molecules on (100) in alkaline medium which increased the compactness of the H_2O layer covering the interface. This hindered the adsorption of molecular O_2 on the surface required for $4e^-$ transfer. For the non-noble metals which develop an oxide film on immersion in aqueous media, OHP mechanism was most likely to occur as manifested by a large ring current during RRDE analysis. This however leads to

View Article Online
DOI: 10.1039/C5CY02270C

ORR by inefficient 2 electron transfer and in order to increase the faradaic efficiency it is vital to promote the IHP electron transfer mechanism at the surface of the catalyst. [83]

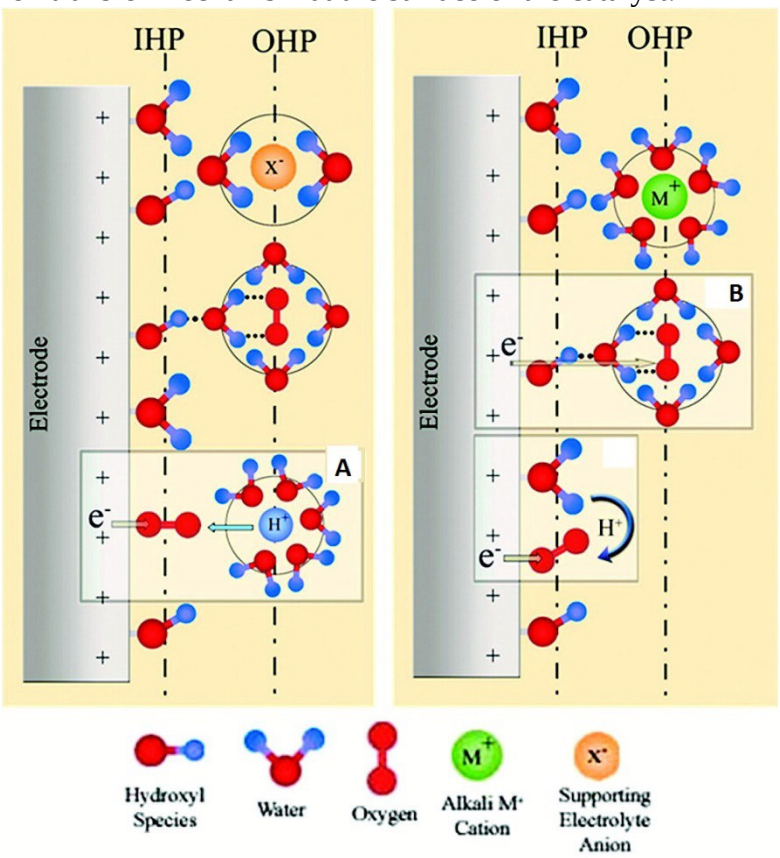

Figure 3 Schematic illustration of the double-layer structure during ORR in acidic (left) and alkaline (right) conditions. Insets (A) and (B) illustrate the inner- and outer-sphere electron transfer processes. Reprinted with permission from ref. 81. Copyright 2011 American Chemical Society.

2.4 Particle Size Effect

The catalytic activity of Ag increases with decreasing particle size. Li *et al.* synthesized Ag/C with a size distribution of 2-9 nm. [84] Average particle size was 5.4 nm. The activity for ORR of these nanoparticles (NPs) was compared with commercially available silver nanoparticles with an average size of 27.4 nm. Anion exchange membrane cell made from these two different cathodes revealed a superior activity in terms of higher power density and lower cathode overvoltage for the nanoparticles with average size of 5.4 nm. The same group deposited these nanoparticles on Vulcan XC-72 and performed RRDE and Cyclic voltammetry (CV) to identify the ORR mechanism. [20] The calculated value of n for Ag/ XC-72 and Pt/C were 3.94 and 3.91 respectively. A comparison of the Tafel plots of Ag/XC-72 with Pt/C revealed 2 distinct regions. A slope of 50.4 mV/dec and 46 mV/dec in the low overpotential region for Ag/XC-72 and Pt/C respectively followed by a Tafel slope of 125.4 and 128.5 mV/decade in the high overpotential region is obtained for Ag/XC-72 and Pt/C (Figure 2). The similar Tafel plots marks a similar mechanism of ORR on these catalysts. A similar comparison of nanoparticles with polycrystalline (PC) silver for ORR was carried by Singh and Buttry. [85] Ag NPs with an average diameter of 4.5 nm were compared with polycrystalline Ag by CV and RDE in 0.1 M NaOH. Analysis of Koutecky−Levich (K−L) plots reveal an electron transfer number from 3-4 for the two catalysts with the higher numbers for the Ag NPs. The lower n number for the bulk Ag was attributed to the more defective surface which leads to stronger adsorption of hydroxyl intermediate which impeded the ORR kinetics. A similar size effect on activity was determined by Lu and Chen on Ag nanoclusters. [86] Both the 0.7 nm and the 3.3 nm Ag clusters were deposited onto glassy carbon electrode and characterized for

View Article Online
DOI: 10.1039/C5CY02270C

ORR by CV. Smaller nanocluster showed superior ORR because of a 150 mV positive onset potential and a five times higher current density as compared to the larger counterpart. However, Li *et al.* reported a 4 electron pathway on the larger 174 nm Ag NPs while a 2 electron transfer path to be prevailing on the 4.1 nm size NPs. [21]

2.5 Morphology Effect

Morphology of the silver nanoparticles has a pronounced effect on the ORR mechanism. Ohyama *et al.* investigated reaction mechanism on three distinct NPs shapes such as smooth, worm like with oxidized surface and angular particles with surface Ag_2CO_3. [87] The ORR proceeded with an exchange electron number of 3.8, 3.6 and 3.5 respectively. However the current density based on electrochemical surface area was lower for smooth particles as compared to the particles with a defective surface. Ohyama *et al.* attributed this to the stronger binding of ORR intermediated on the surface of irregular shape particles as compared to the smoother particles. Wang *et al.* synthesized nanoparticles, nanowires and nanobelts by redox reaction of silver acetate and o-anisidine(OA) . [88] Nanobelts were found to be superior as ORR catalyst based on CV and RDE measurements. The electron exchange number for the nanobelts was calculated to be 3.82 showing a 4 electron dominant pathway. Lee *et al.* synthesized Ag nanosheets onto Ti/TiO_2 by electrodeposition and studied their ORR behavior. [89] Nanosheets revealed a larger electrochemical specific area and mass activities as compared to the Ag NPs. Moreover the Tafel plots revealed 2 distinct slopes -60 mV/dec and -120 mV/dec at low and high overpotential respectively. The electron exchange number from RDE tests was found to be 3.97. All this supporting a 4 electrons transfer path. One dimensional silver rods were synthesized and characterized by Chen *et al.*[90] The Ag nanorods with the ligand-free surface revealed better oxygen reduction characteristics based on CV and RDE studies. The nanorods with surface polyvinylpyrrolidone (PVP) were marked with two plateaus due to peroxide formation while the PVP-free nanorods had a single plateau in their rotating disc polarization plots. Similar one dimensional structure such as silver nanowires was also found to be active and stable towards ORR in alkaline media. [91]

2.6 Alloying Effect

The mechanism of ORR on a catalyst surface is significantly affected by alloying. X-ray absorption near-edge spectroscopy (XANES) and Extended X-ray absorption fine structure (EXAFS) measurements indicate that alloying Pt with metals such as Cr, Co, and Ni take away the charge from Pt and lead to reduced adsorption strength. [92] As a result the coverage by OH from water activation decreases which results in increase in the number of free sites for O_2 adsorption. Furthermore, the weaker adsorption on Pt in the Pt alloys implies a quicker reduction of the oxygenated intermediates during the ORR. The enhanced ORR of Pt_3M (M=Ni, Co) was explained as a result of the enhanced d-band vacancy. Norkosov *et al.* put forward a comprehensive theory, i.e., d-band center, in determining the catalytic activity of metal surfaces, the strength of adsorption of a catalyst was related to its d-band center. [93] The catalytic activity of alloys can be tuned by the adjustment of their d-band centers. This proposition of relationship of activity of a catalyst with its d-band center has been confirmed in both platinum and non-platinum alloys. [94-100] Lima *et al.* found that the platinum group metal (PGM) along with Ag displayed a volcano-type relationship between the alkaline ORR activity and the d-band center. [101] The volcano relationship and the similar Tafel behavior, reveals the similar mechanism of oxygen reduction on these metals. On surfaces with low-energy d-band centers such as Ag, adsorption of oxygen is relatively weak, leading to poor O_2 bond scission. On the other hand surfaces with high-energy d-band centers can readily break O_2 bonds, but results in forming strongly bound O and OH species. Pt and Pd, having intermediate adsorption characteristics, therefore have the highest ORR activity of the Pt-group metals. It is widely regarded that a 0.1 eV decrease in oxygen binding of Pt will lead to the optimum ORR characteristics by DFT and experiment. [32, 42, 102] On the other hand ORR on

View Article Online
DOI: 10.1039/C5CY02270C

silver is sluggish because of its too weak binding with ORR intermediates. To develop active and stable electrocatalysts for ORR a myriad of multi-metallic alloy compositions have been proposed in a variety of structures such as core-shell, skin alloys, thin films, ordered intermetallic and solid solutions. Skin alloys have been widely popular because of their superior activity as compared to the bulk alloys with minimum loading of precious metal which imparts both activity and stability. The enhancement in the activity of these skin alloys is attributed to the geometric and ligand effect of the subsurface atoms on the skin. Subsurface monolayer has also been reported to improve the ORR performance of the silver based alloys.[103] The subsurface transition metal layer has been observed to modulate the surface electronic structure in a manner which improves the ORR kinetics in near surface alloys of silver. The d-band center of the surface in skin alloys is altered by the underlying core because of geometric and ligand phenomenon. The geometric effect can be understood in terms of increase orbital overlap if the skin is in compression. This increase orbital overlap lowers the d-band center and consequently decreases the adsorption energy of adsorbates on the surface of the catalyst. [104-106] The tension in the skin will lead to the opposite i.e. decreased overlap and raised d-band center. The ligand effect results because of the difference in electronegativity of the skin and core.[107, 108] Electrons can migrate towards or away from the skin depending of the electronegativity difference and as a result, occupancy of the local d-band can be varied with the associated change in the adsorption strength of adsorbates. Bard *et al.* proposed guidelines for the design of multimetallic systems for ORR. [109] The model employs the mechanism in which one of the constituent metals easily breaks the O=O bond and the second metals reduces the M-O formed. Based on thermodynamic guidelines a variety of compositions were identified and evaluated by scanning electrochemical microscopy (SECM). Addition of 10-30% of Co to M (M= Ag, Pd and Au) was found to improve the catalytic activity for ORR of these alloys.

2.7 Support Effect

Catalyst support plays a crucial role in stability and functionality of catalyst during ORR. Stability is imparted to the catalyst by avoiding nanoparticle agglomeration under fuel cell operating conditions. [110] Catalyst support such as carbon black allows gas diffusion to the active sites along with electronic conductivity which permits electron transfer from catalytic sites to the conductive electrodes. The dispersion of catalyst particles on a carbon support maximizes the contact area between catalyst and reagents. ORR occurs only at those sites where the three phases i.e. reactant-electrolyte-catalyst meet. This is because of the fact that the solubility and diffusivities of oxygen in aqueous electrolytes is low. Porous gas diffusion electrodes are employed in the aqueous Zn-air battery to optimize the three phase contact and sustain high current density. [111-113] Silver nanoparticles on graphene oxide (GO) and graphene oxide/carbon were developed to investigate their ORR performance in alkaline environment. [114] The composites were facialy synthesized by the reduction of $AgNO_3$ with graphene oxide with or without the presence of Vulcan XC-72 carbon black. The average particle size of Ag/GO/C composites (ca d = 12.9 nm) was found to be almost twice of Ag/GO composite (ca d = 6.9 nm). The nanocatalysts were electrochemically characterized which revealed the superior performance of Ag/GO/C for ORR as compared to Ag/GO. RDE analysis revealed that the onset potential and the half wave potential shift positively for Ag/GO/C as compared to Ag/GO. This enhancement in ORR performance was attributed to the 3D composite support which not only improves the electrical conductivity but also facilitated the mass transport in the catalyst layer. A similar beneficial effect of catalyst support was observed in the case of $Ag/Mn_3O_4/C$ catalysts (Figure 4). [98] The catalyst performance for ORR in alkaline media was found to be superior to the simple Ag/C catalyst. This improvement was ascribed to the Mn_3O_4 support which perturbed the electronic structure of the silver particles. Charge was transferred to Mn_3O_4 support from Ag which was manifested by the lowering of the binding energy of the Ag 3d electrons in X-ray photoelectron spectroscopy (XPS) measurements. This was accompanied with the rise of the d-band center of Ag in the $Ag/Mn_3O_4/C$ catalyst as compared to the Ag/C catalyst. Higher current density, electron transfer numbers and more positive onset

View Article Online
DOI: 10.1039/C5CY02270C

potentials have been found for the co-support of Ag with Mn_xO_y or Co_3O_4 on carbon compared to only Ag/C. [72, 115-119]

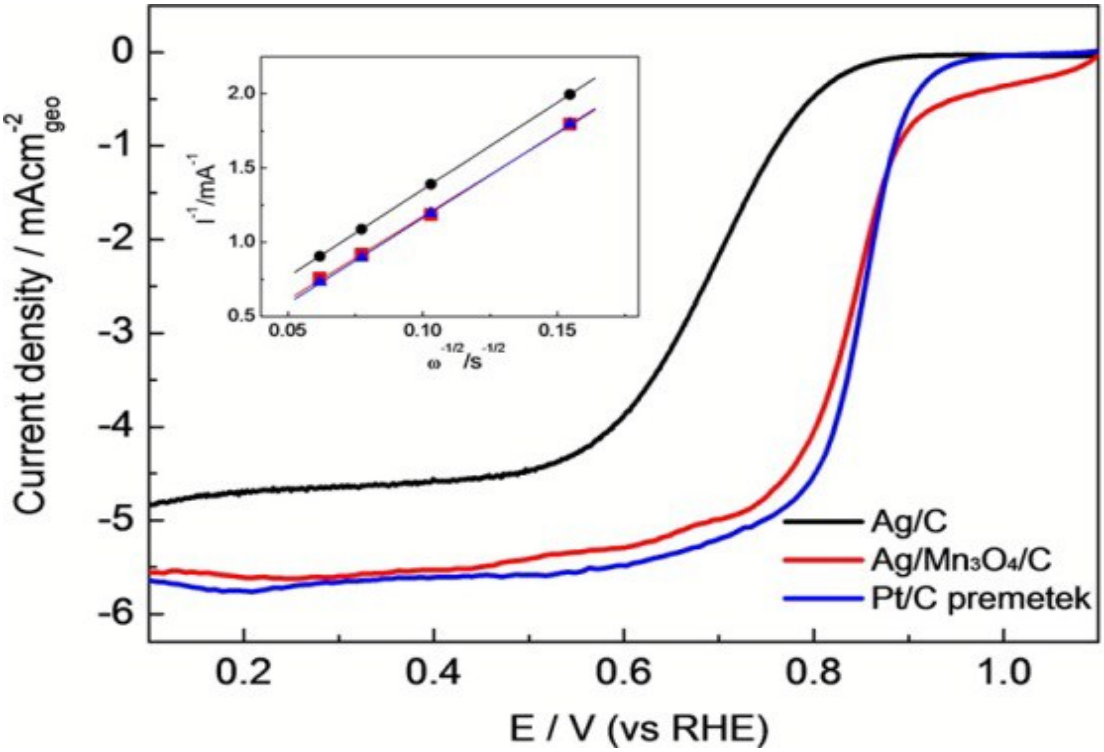

Figure 4 Oxygen reduction polarization curves for Ag/C, Ag/Mn_3O_4/C, and Pt/C premetek at 1600 rpm in O_2-saturated 0.1 M KOH at 10 mV/s, and (inset) Koutecky–Levich plots for ORR in the presence of Ag/C, Ag/Mn_3O_4/C, and Pt/C premetek at 0.32 V vs. RHE. Reprinted with permission from ref. 98. Copyright 2015 American Chemical Society.

3 Silver Nanoalloys.

3.1 Ag-Cu Nanoalloys

The Ag-Cu system is an interesting system because of the fact that silver and copper are immiscible in the bulk, but possibly miscible in the nanoscale. In the nanometer size range the system preferentially adopts the $Ag_{shell}Cu_{core}$ arrangement. [120, 121] Theoretical studies performed on the Ag_{y-x}-Cu_x nanoalloy system have been performed for all compositions of 13, 34, 38 and 98 atoms Ag-Cu nanoalloy clusters. These studies showed that the most stable structures are generally core-shell polyicosahedra for x= 1, 7 and 6 and y= 13, 34 and 38 having a Cu core embedded in a Ag shell. [121, 122] The stability of polyicosahedra core-shell geometry originates from the interplay of size mismatch, bond order-bond length correlation, and the tendency for surface segregation of Ag, due to the lower surface energy of Ag compared to Cu. [123]

Ag-Cu nanoalloy clusters have revealed improved ORR activity as compared to pure Ag and Cu. [35, 36, 124, 125] Ma *et al.* performed first principle calculations for the ORR process in alkaline media on the 13 atom pure Ag and Cu doped Ag clusters. [124] 13 atom Ag-Cu nanoalloy clusters have been previously identified as a potential catalyst for ORR. [35] Pure Ag_{13} and $Ag_{12}Cu_{surface}$ clusters with cuboctahedron (COh) symmetry were used for these calculations. The doping of copper significantly improves the ORR process. The ORR reaction was observed to occur by the efficient four electron transfer mechanism. Doping of silver with copper atom on the surface improves the binding of the intermediates such as O, OH, and OOH on the nanoalloy cluster. This optimum binding is critical for the efficient ORR. The stronger binding of the intermediates on $Ag_{12}Cu$ cluster compared to pure Ag is the reason behind the better ORR performance of $Ag_{12}Cu$ cluster. The $Ag_{38-x}Cu_x$ cluster has been studied for the ORR by Lee

View Article Online
DOI: 10.1039/C5CY02270C

et al. [36, 126, 127] Truncated Octahedron (TO) $Ag_{32}Cu_6$ alloy cluster was observed to perform as a better catalyst for ORR as compared to the TO $Ag_{32}Cu_6$ core-shell clusters. However, Zhang *et al.* reported that the stability of polyicosahedron (PIh) $Ag_{32}Cu_6$ core-shell structure exceeds that of TO $Ag_{32}Cu_6$ core-shell by 0.564 eV and Truncated Octahedron (TO) was the most stable geometry for the pure Ag_{38} and Cu_{38} clusters. [125] The polyicosahedron (PIh) $Ag_{32}Cu_6$ core-shell structure was further investigated for the ORR. ORR was found to proceed by the dissociation mechanism as compared to the associative mechanism by 0.1 eV. Hence dissociative ORR mechanism involving the scission of molecular oxygen to atomic form i.e. $\boldsymbol{O_2 \rightarrow O + O}$ was considered for the computational analysis. Four active sites were identified on the $Ag_{32}Cu_6$ core-shell structure as B1 to B4. The ORR was then followed with the bond fracture and subsequent adsorption of atomic oxygen at hollow sites marked H1, H2 and H3 (Figure 5A). In order to explain further that B2 site is most favorable to display a good catalytic behavior, the electronic structure of these four adsorption configurations was addressed and the position of the d-band center relative to the Fermi energy for these different sites was calculated (Figure 5B). The d-band center of B2 site is -3.395 eV, which is closest to the Fermi Level. By having the dband center closest to the Fermi level as compared to the other adsorption sites on the polyicosahedron (pIh) $Ag_{32}Cu_6$ core-shell structure, B2 site is the most conducive for ORR as it enhances the otherwise weak affinity of silver alloys for the reaction intermediates. Frontier orbital theory describes that the states of a metal which are involved in electron transfer with the adsorbates are ones which are closest to the Fermi Level. [128] Therefore, the density of states (DOS) at the Fermi level is an indicator of the chemical activity. We notice that the density of states at the Fermi energy level is maximal for B2 site. This further endorses the superior activity of the B2 site for the ORR on $Ag_{32}Cu_6$ core-shell nanoalloy.

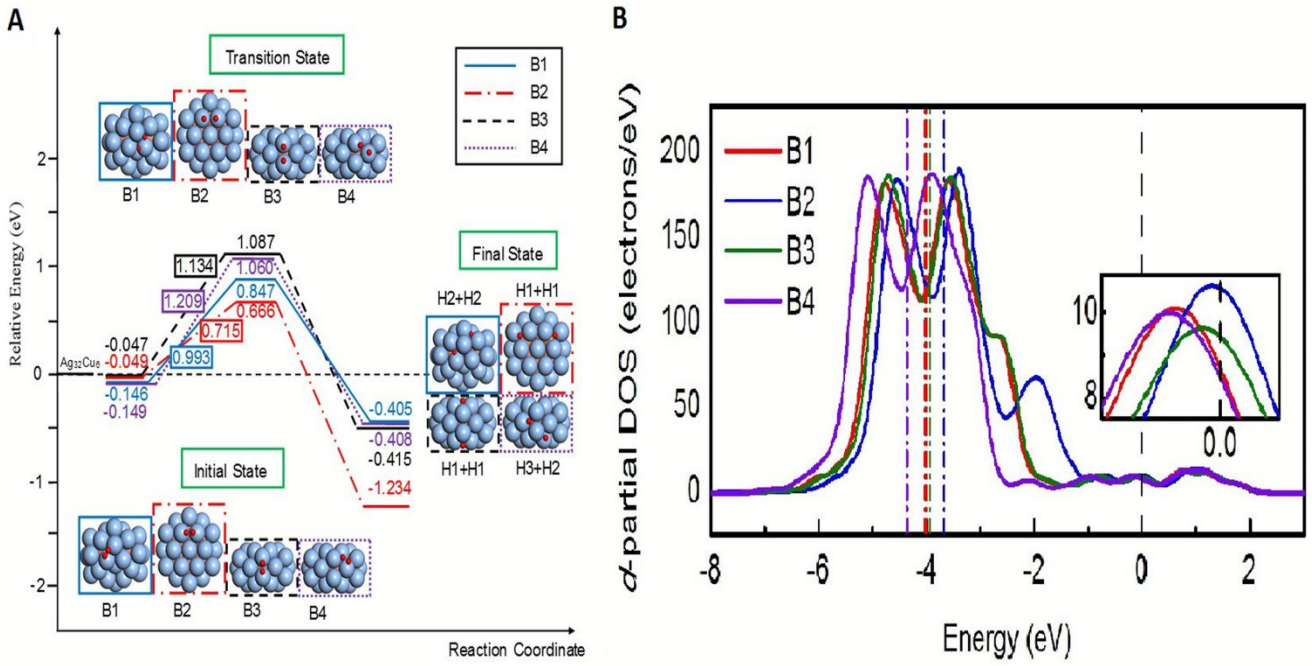

Figure 5 **ORR on pIh $Ag_{32}Cu_6$ core-shell cluster** (A) Profiles of potential-energy surfaces of four oxygen dissociation pathways on the pIh $Ag_{32}Cu_6$ core-shell cluster. (B) Center of d-band and density of states at the Fermi level (inset) of four O_2-cluster adsorption configurations. Adapted with permission from ref. 125.

Ag-Cu nanoalloy catalysts have also been developed by physical laser deposition (PLD) method in a vacuum chamber. [129, 130] The target of Ag-Cu alloy with atomic ratio of 50:50 was irradiated with a nanosecond Q-switched neodymium-doped yttrium aluminium garnet **(**Nd:YAG) laser beam. The as-prepared product is $Ag_{50}Cu_{50}$ catalyst. Figure 6 shows series of transmission electron microscopy (TEM) analysis on $Ag_{50}Cu_{50}$ catalyst. Plenty of nanoparticles are distributed in a continuous film. The

View Article Online
DOI: 10.1039/C5CY02270C

tiny nanoparticles with size under 5 nm dominate the film. Magnifying the blue rectangle area, the obtained High resolution transmission electron microscopy (HRTEM) is shown (Figure 6B) in which it can be seen that they display two different states: few are amorphous and some with crystallized state. High-Angle Annular Dark Field (HAADF) images display that contrast of the particles is brighter than gap area between particles, demonstrating a higher atomic number Z for nanoparticles (Figure 6C). The lower Z corresponding gap area then is attributed from Cu element. This is because Z=29 of Cu is smaller than Ag (Z = 47). Combining the amorphous state in gap area observed, we can draw that $Ag_{50}Cu_{50}$ catalyst actually is Ag-Cu alloyed nanoparticles embedded in amorphous Cu film (Figure 6B). Figure 6E shows a set of RDE curves with rotation rates of 400, 800, 1,200, and 1,600 rpm in 0.1 M KOH. The Koutecky-Levich plots were then obtained from the limiting current density (Figure 6E inset). The plots show the inverse current density J^{-1} as a function of $\omega^{-1/2}$. From these plots the number of electrons transferred during ORR was found to be 3.76, 3.87, 3.85, and 3.97 when the potential was 0.5, 0.4, 0.3, and 0.2 V, respectively. Hence four electrons route was found to be the dominant for ORR in case of synthesized $Ag_{50}Cu_{50}$ catalyst. Figure 6F gives a comparison of the performance of Ag, $Ag_{50}Cu_{50}$ and Pt/C(20 wt%). Very recently a highly active and stable Ag-Cu metallic glass deposited by PLD on Ni-foam for ORR has been reported. [131] The half wave potential of this Ag-Cu system was found to be improved to 0.78 V from 0.67 V vs. RHE by in-situ dealloying treatment in N_2-saturated 0.1 M KOH. Dealloying treatment of Ag-Cu lead to an increase in the number of active sites for ORR in alkaline media which rendered this carbon free binder free system half wave potential comparable to commercial Pt/C.(0.81 V vs. RHE @ 1600 rpm in 0.1 M KOH)

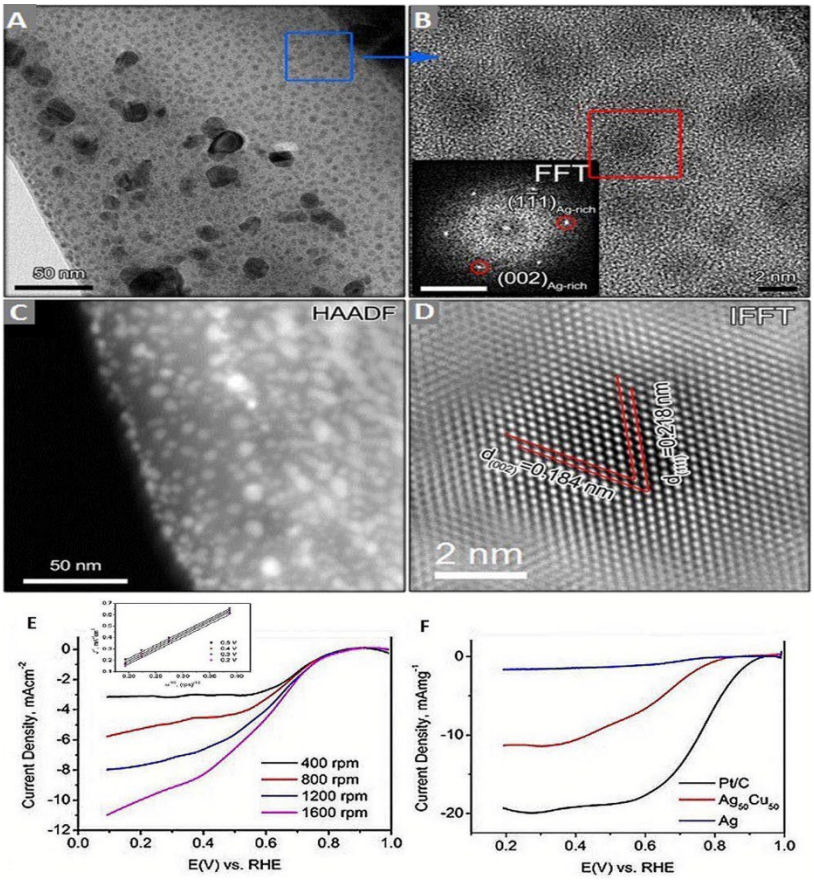

Figure 6 Characterization of $Ag_{50}Cu_{50}$ catalysts. (A) Bright field TEM image, (B) HRTEM, (C) HAADF result, and (D) IFFT image. The scale bar for the inset FFT image in (B) is 5 nm. (E) the RDE curves at the rotation rates of 400, 800, 1,200, and 1,600 rpm (inset) Koutecky-Levich plot of $Ag_{50}Cu_{50}$ catalyst and (F) the ORR mass activity for Ag, $Ag_{50}Cu_{50}$, and Pt/C (20 wt%) catalysts. Adapted with permission from ref. 129.

View Article Online
DOI: 10.1039/C5CY02270C

Ag-Cu catalysts have also been synthesized directly on Ni foams by galvanic displacement reaction. [132] In this method, the catalysts were directly grown on Ni foams, thereby freeing the catalytic layer from carbon and binder. The driving mechanism to grow the various catalysts by galvanic displacement is the large difference of the redox potentials of Ni^{2+}/Ni (–0.25 V vs. SHE), Cu^{2+}/Cu (0.34 V vs. SHE), and Ag^{+}/Ag (0.799 V vs. SHE). RDE measurements were performed on the catalysts made by galvanic displacement and comparison was made with pure silver. AgCu-10 nanoalloy performed efficiently as compared to the pure silver particles in terms of both onset potential and the limiting current. The koutecky-Levich plots revealed the 4 electron transfer mechanism during the ORR. The rechargeable zinc-air battery made with the AgCu-10 nanoalloy show high cycling stability at the long cycle period. The increasing of charge and discharge potentials difference from the first to tenth cycle was observed as little as 0.06 V, which is comparable to the tri-electrode rechargeable zinc-air battery. [133] Ag–Cu catalysts were also synthesized by the electro-deposition method under a potential of −0.4 V for a period of 50 s by using the conventional three-electrode cell system. [134] The nanoplatelets produced had diameters of 40–50 nm. The lattice spacing obtained from the HRTEM image was 0.239 nm. The particle demonstrated a single crystal pattern in the selected area electron diffraction (SAED) , indicating Ag-Cu catalysts grew larger by the oriented attachment from small Ag–Cu nanoparticles. The cell constant of the single crystal was 0.3986 nm, which is between the standard cell parameter of FCC-Ag (a = 0.4086 nm) and FCC-Cu (a = 0.3615 nm), suggesting that the Cu atoms were partially alloyed with the Ag atoms. To study the catalysis kinetics of Ag–Cu catalyst for ORR, RDE experiment was performed in O_2-saturated 0.1 M KOH solution. The number (n) of electrons transferred on the Ag–Cu catalyst during ORR was determined by the Koutecky–Levich plots. The result indicated that the ORR was catalyzed by the Ag–Cu catalyst through a four-electron pathway.

Alkaline Fuel cells and metal-air batteries are prone to the carbonation of electrolyte which arises from the reaction of CO_2 in air with electrolyte. Carbonation reduces the electrolytes conductivity and can choke pores of the air electrode as well. However, Ag-Cu nanocatalyst exhibits a good tolerance towards CO_2. CO_2 tolerance of the primary Zn-air battery made from Ag-Cu nanocatalyst electro-deposited on Ni-foam was monitored by adding different amounts of K_2CO_3 to the KOH electrolyte. [134] Addition of 0.5 M K_2CO_3 in 6 M KOH lead to a slight decrease of 3.8% in the maximum power density along with a small 0.68% decrease in discharge voltage at 20 mA/cm^2. Further raising the concentration of K_2CO_3 in 6 M KOH to 1 M, the discharge voltage was observed to be 97.5% of the K_2CO_3 free solution. These results demonstrate the tolerance of electrodeposited Ag-Cu nanoalloy based primary Zn-air battery towards CO_2. The problem of CO_2 poisoning of AFCs and metal-air batteries can be further addressed by its flow management. CO_2 from the ambient air can be filtered by the use of Scrubbers made of soda lime or amines such as monoethanolamine. [135, 136] It is reported that a kilogram of soda lime can clean 1000 m^3 of air, taking the CO_2 level from 0.03% to 0.001%. [137] Moreover techniques such as replacing the electrolyte periodically and operating the fuel cells at slightly higher temperatures (60-80 ^{o}C) are also reported for the control of CO_2 poisoning. [138]

3.2 Ag-Pd Nanoalloys

Silver and palladium are fully miscible in the bulk forming no ordered phases. [139] However chemical reduction of mixed solutions of Ag and Pd salts lead to formation of core-shell nanoalloys. $Ag_{shell}Pd_{core}$ and $Ag_{core}Pd_{shell}$ nanoparticles have been produced by underpotential deposition (UPD) of Ag adatoms onto Pd and by galvanic displacement method. [140, 141] Pd coated silver nanoalloy was synthesized by galvanic displacement reaction by Jiang *et al.*[142] Catalytic performance of Pd@Ag/C alloy was compared with commercial Pt/C (20 wt.% Pt). Pd@Ag/C showed a 3 and 2.5 times superior specific and mass activity respectively as compared to the Pt/C catalyst. From the comparison of the Tafel plots a similar reaction mechanism was found on both Pd@Ag/C and commercial Pt/C catalyst. First electron transfer was found to be the rate determining step in the low over potential region. Pd@Ag/C tolerance

View Article Online
DOI: 10.1039/C5CY02270C

towards ethanol oxidation reaction (EOR) was monitored by performing rotating disc voltammetry in a 0.1 M NaOH+0.01 M ethanol solution. Pd@Ag/C revealed selectivity towards ORR while EOR was observed on commercial Pt/C catalyst. $Ag_{core}Pd_{shell}$ nanoalloy particles were developed on 1-D multi walled carbon nanotube (Ag@Pd/MWNT) by galvanic displacement of silver. [143] Ag@Pd/MWNT nanoparticles with an average particle size of 7.5 nm were produced. Average number of electrons transferred during ORR in 1 M KOH was found to be ~3 for this nanocatalyst. This implies both $2e^-$ and $4e^-$ pathways to be active during oxygen reduction on Ag@Pd/MWNT. Ag@Pd/MWNT showed current density of -5.6 mA/cm^2 at -0.4 V vs. Hg/HgO compared to -3.13 mA/cm^2 for Ag/MWNT. The core-shell ensemble imparted superior activity to the Ag@Pd/MWNT. Moreover unlike Pt/C, Ag@Pd/MWNT was found to be tolerant to ethanol and methanol and hence a prime candidate as a catalyst for the direct alcohol fuel cells. Ag-rich AgPd nanoalloy particles with crystalline morphology were synthesized by simultaneous thermolysis of organometallic precursors. [144] Ag_9Pd particles were uniformly alloyed with a particle size of 5.3 nm (Figure 7A). The monodisperse particle size was attributed to the similar reduction rates of the metal precursors. X-ray diffraction (XRD) peak for {111} planes is located between both pure Pd and Ag showing the alloying with 10 mol% Pd (Figure 7B). The lack of additional peak shoulders suggests that the particles are composed of a single alloy phase, Ag_9Pd. This notion is further confirmed by the scanning transmission electron microscope (STEM) energy dispersive X-ray spectroscopy line scan which shows good intermixing of Ag and Pd in nanoalloy (Figure 7, C and D). ORR analysis via RDE and CV revealed a 4 electron transfer pathway for the Ag_9Pd/Vulcan XC-72 nanoalloy catalyst (Figure 7E). The activity enhancement was found to be non-linear with maximum boost for the Ag_4Pd and Ag_9Pd nanoalloys. The synergy effect due to the Ag and Pd in the AgPd nanoalloy resulted in a Pd mass normalized activity of 4.7 times over the commercial Pd/Vulcan XC-72 and up to 3.2 times over the linear combination of mass activities for pure Ag and Pd (Figure 7F). By the addition of 10 mol% Pd in Ag the onset potential for the Ag_9Pd nanoalloy shifted positively by nearly 100 mV. The ligand effect due to the d-band modification of AgPd nanoalloy was found to play a minimal role in this enhancement of activity. Rather an ensemble effect similar to one proposed by Bard *et al.* was reported as the reason of the superior activity of AgPd nanoalloys. [109] This ensemble effect originated from a suitable geometric arrangement of Ag next to Pd surface atoms to catalyze the ORR. By creating AgPd alloy surface, the Pd atoms facilitate the initial oxygen binding whereas the Ag helped to desorb the reaction products such as OH^-. For PdAg surface, DFT calculations suggest Pd sites to be the most likely spot for oxygen adsorption. [145] Molecular oxygen may bind at the Pd sites, with one oxygen atom onto the Ag site. The ensemble of Pd and Ag on the nanoalloy surface was proposed to lead to complete reduction of dioxygen.

Silver palladium nanoalloys have also been reported in innovative shapes such as hollow rings and triangular prisms. [146, 147] Hollow ring silver palladium nanoalloys were made by galvanic displacement of silver on graphene support. TEM revealed a ring diameter of 27.5 nm with a thickness of 5.5 nm. Alloying of silver and palladium was confirmed by XRD, XPS and HRTEM data analysis. Ag-Pd nanorings were found to be more active towards ORR by RDE and CV tests. The tolerance of Ag-Pd nanorings towards methanol was examined by performing ORR in 0.1 M KOH solutions with increasing concentrations of methanol from 0.5 M to 5 M. No decrease in reduction currents manifested the methanol tolerance of the nanorings. Ag-Pd nanoalloy prisms with superior activity for ORR compared to Pd/C were synthesized by a galvanic displacement of Ag. The nanoalloy prisms had an average edge length of 90 nm. Energy dispersive X-ray spectroscopy (EDX) revealed the uniform distribution of Ag and Pd in the nanoprisms. The XRD peaks of the nanoprisms were located between those of pure Ag and Pd revealing the alloying in the Ag-Pd nanoprisms. RDE tests on the Ag-Pd nanoprisms confirmed their superior activity with reference to commercial Pd/C catalyst. ORR proceeded with an electron exchange number of 3.84, marking the dominance of $4e^-$ transfer pathway. The authors attributed the enhanced activity of Ag-Pd nanoalloy prisms to uniform alloying which yielded synergistic effect, {111} facets with the optimum OH^- binding strength and porous features. Ag/Pd triangular nanoplates

View Article Online
DOI: 10.1039/C5CY02270C

with different alloy ratios $Ag_{18}Pd_1$, $Ag_{18}Pd_{1.5}$, and $Ag_{18}Pd_2$, were prepared by galvanic displacement reaction. [148] Mass activity was found in the order $Ag_{18}Pd_1$>$Ag_{18}Pd_2$>$Ag_{18}Pd_{1.5}$>Pt NPs>Pd NPs. From the Koutecky Levich plots electron exchange number was calculated to be 3.5. Tafel plots were marked with two distinct slopes of -60 mV/dec and -120 mV/dec . The porous Ag/Pd triangular nanoplates were found to be tolerant towards methanol sensitivity. The high activity and stability of these Ag/Pd triangular nanoplates in alkaline media make them a strong candidate for the direct alcohol alkaline fuel cells. Recently 1-Dimensinonal AgPd nanoalloy based AgPd-Pd porous nanotubes have been reported to have higher catalytic activity than commercial Pt/C for ORR even in the non-aqueous environment. [149] AgPd-Pd composite were synthesized by galvanic displacement method. Nanoalloy AgPd layer in these nanoporous composite was identified to be vital for the improved ORR activity of the electrocatalyst.

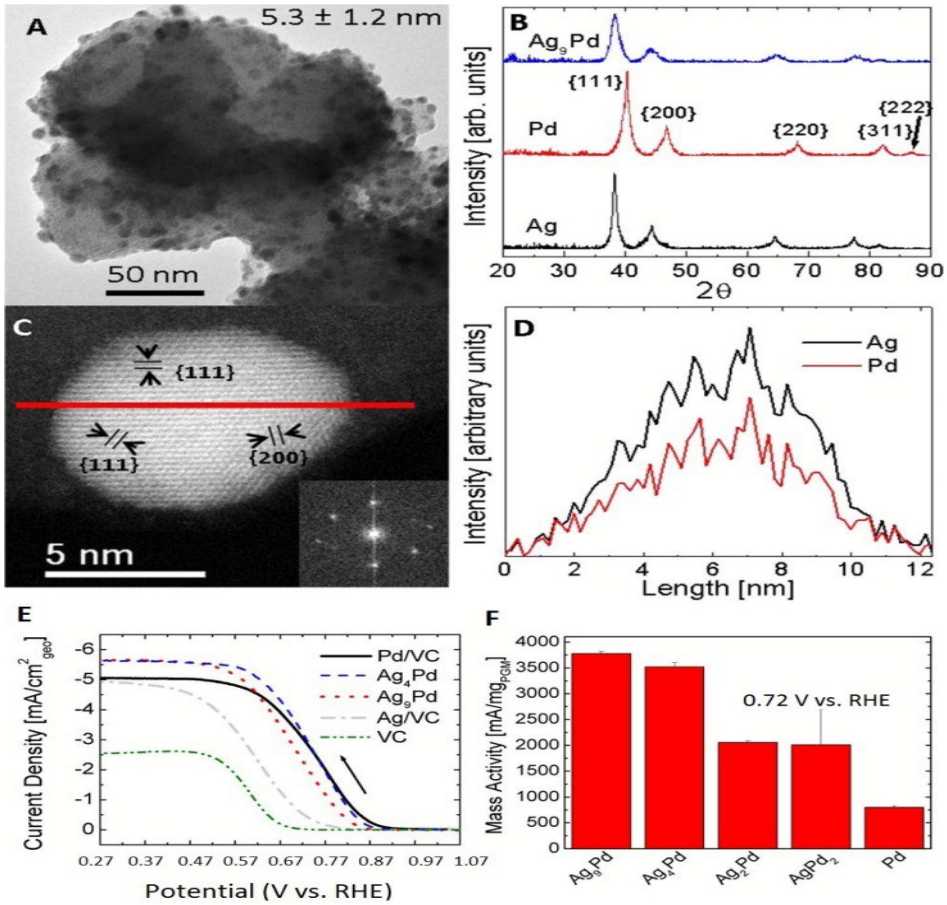

Figure 7 Ag_9Pd nanoparticles supported on Vulcan XC72 carbon after calcination at 350 °C in N_2. (A) TEM and (B) XRD. The TEM shows that the particles are uniformly distributed over Vulcan XC72 with an average particle size of 5.3 ± 1.2 nm. The uniform composition is confirmed by the STEM EDX line scan (C,D). Furthermore, the particles are shown to be composed primarily of {111} facets (C, inset), along with twinning for the {111}.(E) Linear sweep voltammograms from a rotating disk electrode measurement in O_2 saturated 0.1 M KOH. (F)Bar plot summarizing the ORR activity per Pd loading. The synergy between the Ag and Pd in the alloy achieves a Pd mass normalized activity of 4.7× over the commercial Pd/VC and up to 3.2× over the linear combination of mass activities for pure Ag and Pd. Adapted with permission from ref. 144. Copyright 2012 American Chemical Society.

3.3 Ag-Au Nanoalloys

Like the Ag-Pd system, Ag-Au form solid solutions for all compositions in the bulk systems. [150] The lattice constants of the two constituent metals are very close to each other and both metals form FCC crystal structures. The electronic structures and chemical properties are also similar, resulting in fairly weak interactions between the gold and silver atoms. The mixing of Ag and Au in the bulk is weakly

View Article Online
DOI: 10.1039/C5CY02270C

exothermic, and there is believed to be very little surface segregation in bulk Ag-Au alloys. However, core-shell particles have been produced by laser irradiation as well as by chemical deposition of one metal onto a preformed cluster of the second one. [151-154] Ag-Au bimetallic Janus nanoparticles with enhanced electrocatalytic activity for oxygen reduction were prepared by interfacial galvanic exchange reactions of Ag-C6 nanoparticles with gold(I)-mercaptopropanediol (AuI-MPD) complex. [155] A monolayer of 1-hexanethiolate-passivated silver (AgC6) was deposited onto a glass slide surface by the Langmuir−Blodgett method, which was then immersed into a solution of AuI-MPD complex. Controlled galvanic displacement reactions between the AgC6 nanoparticles and AuI-MPD led to the displacement of part of the Ag atoms on the nanoparticle cores with Au lead to formation of AgAu bimetallic Janus nanoparticles with the capping agents in assymteric distribution (Figure 8A). The galvanic displacement was concurrent with the replacement of the original hydrophobic hexanethiolates with the more hydrophilic MPD ligands. A modified displacement method employing stirring resulted in homogeneously mixed AgAu nanoparticles (Figure 8B). From TEM, average core diameter was found to be 5.79 ± 1.02 and 5.36 ± 0.85 nm for the uniformly mixed and Janus particles respectively. Moreover, the nanoparticles exhibited well-defined crystalline lattice fringes with a spacing of 0.235 nm that may be ascribed to the (111) planes of both FCC silver and gold. RRDE voltammaograms were carried in 0.1 M NaOH to investigate the ORR activity of the AgC6, homogeneously mixed and janus AgAu nanoparticles (Figure 8, C to E). Onset potential for the oxygen reduction reactions moved to positive value of +0.917 V vs. RHE for the Janus AgAu nanoparticles compared to the +0.809 V vs. RHE for the uniformly mixed AgAu nanoparticles. The amount of hydrogen peroxide generated during the oxygen reduction is indicative of the ORR pathway. Percentage of peroxide at ring was higher for the uniformly mixed compared to the janus nanoparticles. Koutecky-Levich data revealed an electron exchange number of 3.15 ± 0.10 for the bulk-exchange, and 3.36 ± 0.03 for the Janus nanoparticles within the potential range of +0.2 to +0.6 V vs. RHE. The RRDE data suggested a $4e^-$ transfer pathway to be dominant for the AgAu janus nanoparticles. Area-specific kinetic current density at +0.68 V vs. RHE was estimated to be 8.75 A/m^2 for the uniformly mixed particles and 40.64 A/m^2 for the Janus nanoparticles. It was observed that the current density of the uniformly mixed nanoparticles was only about 50% higher than that of AgC6 while the activity of the Janus nanoparticles was more than seven times higher.

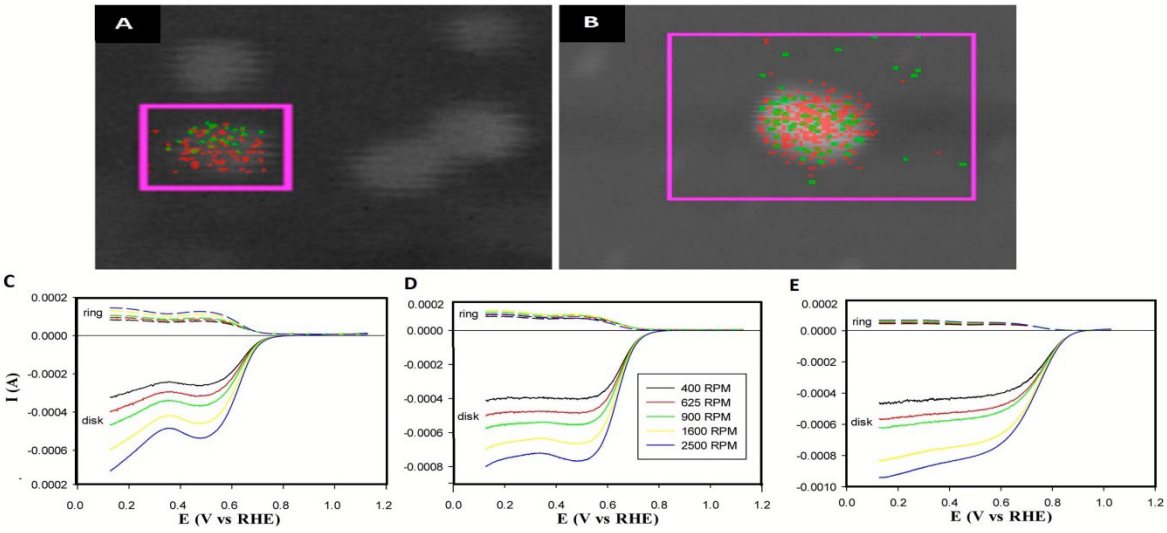

Figure 8 Characterization of AgAu Nanoalloy. Representative false-color EDX elemental maps. (A) Janus and (B) bulk-exchange nanoparticle with red symbols for Ag and green for Au. RRDE voltammograms of a glassy-carbon disk-gold ring electrode (C) as-prepared AgC6, (D) bulk exchange, and (E) Janus nanoparticles in an oxygen-saturated 0.1 M NaOH solution. Electrode potential sweep rate was 10 mV/s, the ring potential was set at +1.4 V, and rotation rates were specified in the figure legends. Adapted with permission from ref. 155. Copyright 2012 American Chemical Society.

View Article Online
DOI: 10.1039/C5CY02270C

Computational screening of silver skin alloys having a monolayer skin of Ag onto the core of 2nd element was performed to enhance the otherwise weak binding of pure oxygen with Ag. [38] Considering binding energy of oxygen as an indicator of reactivity, a number of Ag/M (M= Au, Cu, Ir, Pd, Pt,Os Ru) skin alloys were analyzed by DFT calculations. A peculiar phenomenon of enhancement of oxygen binding of Ag/Au by the more inert Au core under Ag skin was observed. Importantly the skin of Au on Ag (111) significantly weakened the oxygen binding of the alloy. The full d-band of Ag and Au along with close lattice parameters suggested the absence of d-band factor for this enhancement of oxygen binding. [93] The authors attribute this enhancement of activity to the surface effect. [156] Guided by DFT calculations Ag/Au was synthesized by underpotential deposition (UPD) method. Firstly Pb monolayer was deposited on Au electrode in 1 M KOH solution containing 1 mM $Pb(NO_3)_2$, and then replaced the Pb monolayer with Ag by rotating the Pb/Au electrode in a $AgNO_3$ solution (1 mM) for a controlled period of time. RDE measurements in 0.1 M KOH on the Ag skin/ Au Core alloy revealed the superior activity as compared to both pure Ag and Au. The halfway potential ($E_{1/2}$) value of the Au@Ag electrode was 50 mV more positive than that of the usual Ag electrode. The Tafel plots revealed 2 distinct slope regions i.e. -60 mV/dec at low overpotentials and -120 mV/dec at high overpotentials. The similarity of Tafel plots of Au@Ag alloy with Pt reveals a similar ORR mechanism with the first electron transfer as the rate determining step. [56-58] An increase in catalytic activity by half an order of magnitude was reported. Ag-Au nanoalloy particles partially capped with 1-Dodecyne were synthesized by chemical reduction of metal salt precursors. [157] The atomic % of Au was varied in these nanoalloy particles from 26.7 to 51.5. In terms of onset potential, electron exchange number and kinetic current density data acquired from RRDE in 0.1 M KOH, AgAu nanoalloy particles with 35.5 at% Au were the most active towards ORR. The particle size of this composition was measured to be 3.68 nm from TEM. XPS of these nanoparticles confirmed the presence of both Ag and Au in metallic state. The surface plasmon resonance SPR of Ag-Au nanoparticles shifted towards longer wavelength (redshift) with increasing Au content. Also presence of a single plasmon peak supports the conjecture of alloying of Ag and Au in Ag-Au nanoparticles. Minimum amount of peroxide was detected at the ring of RRDE. Koutecky Levich analysis of RRDE for Ag-Au nanoalloys revealed an electron exchange number from 3.8-4.0 for the six different compositions. This supports the notion of $4e^-$ pathway for ORR on AgAu nanoalloy particles. Like the janus AgAu nanoparticles, Tafel plots of these nanoalloys were marked with two distinct regions -60 mV/dec at low overpotentials and -120 mV/dec at high overpotentials. Similarity of Tafel plots with Pt and pure Ag suggest a similar ORR mechanism on the AgAu nanoalloys with the first electron transfer as the rate determining step. The specific activity of AgAu nanoalloys at +0.85 V vs. RHE gave a volcano-shaped variation with the maximum with sample 35.5 at% Au, suggesting that the optimal concentration of Au was about 35.5 at% for ORR. The enhanced activity of Ag-Au nanoalloys was related to the improved surface oxygen absorption. Wang *et al.* have reported an increase of oxygen species on the Ag-Au alloy surface compared to the pure Ag or Au surfaces [158], and the amount of oxygen species varied with different Ag/Au ratios. Therefore the enhancement of ORR performance of Ag-Au nanoalloys was attributed to the improved surface oxygen affinity by alloying Ag and Au, leading to a positive shift of the onset potential accompanied with low peroxide formation and electron exchange number of ~4.

3.4 Ag-TM (M=Co, Ni, Mn) Nanoalloys

The 3d post transition metals (TM) cobalt and nickel which are well-known alloying elements in Pt-based systems, are immiscible with silver in bulk. [159, 160] Theoretical studies of small and large Ag-Co nanoclusters showed that Ag atoms tend to occupy surface sites [161, 162]. DFT studies for Ag-Ni system have validated that Ag atoms tend to occupy surface sites. [163, 164] The surface segregation of Ag in Ag/M (M= Co, Ni) alloys is favored because of lower surface energy of silver E_{Ag} = 1.25 J/m^2 compared to nickel and cobalt, E_{Ni} = 2.38 J/m^2, E_{Co} = 2.52 J/m^2. [123] The smaller atomic sizes of Co and Ni compared to Ag also favor the core occupation by these metals in Ag shell. Since the report of ORR

View Article Online
DOI: 10.1039/C5CY02270C

on bimetallic Ag-Co nanoparticles by Lima *et al.*, very few Ag-Co nanoalloys for ORR in alkaline media have been reported. [165] The reported Ag-Co bimetallic nanoparticles by Lima had little mixing between the Ag and Co as revealed by the presence of cobalt mainly in the form of Co_3O_4 with slight formation of Co_2O_3 by XRD analysis. Also the slight decrease in the lattice parameter of Ag reflected the minimum insertion of Co atoms in Ag. Ag-Co in the form of cobalt islands on top of Ag(111) have been reported to be more active towards ORR compared to the pure Ag. [166] The deposition of Co on Ag involved SLRR (surface layer redox reaction). The 30% Co/Ag(111) was found to be the most active catalyst towards ORR by CV and RDE in 0.1 M KOH. Polyaniline modified binary silver-cobalt catalysts with different Ag_xCo_y ratios for ORR was synthesized by electrodeposition on Ti. [167] ORR on PANI(15)-$Ag_{31}Co_{69}$/Ti occurred with onset potential of 0 V (vs. Ag/AgCl) and a high ORR current density of 1.2 $mAcm^{-2}$ at -0.12 V (vs. Ag/AgCl). The electrocatalyst was found to be tolerant to methanol and ethanol oxidation and can be employed in direct alcohol fuel cells. Addition of Co to Ag resulting in improved ORR performance has been reported by Zafferoni *et al.* [168] The activity in of Ag-Co catalyst was reported to be on the same order of magnitude but with slightly lower values as compared to Pt/Vulcan.

Ag-Co near surface alloy nanoparticles with area specific activity more than five times than pure silver and about half of Pt were designed by the aid of quantum chemical DFT calculations. [103] Reaction Free energy diagram for Pt(111), Ag(111) and subsurface Ag alloys with transition metals was constructed (Figure 9A). The rate limiting step for Ag and its alloys in the working potentials and pH was found to be the first electron transfer for the formation of OOH*. This was different from Pt(111) in which the excess coverage of OH* posed a barrier for the final OH^- formation. Guided by DFT calculations an Ag-Co alloy was developed by rapid heating of metallic salts at 500 ^oC. Subsequent leaching of this binary alloy removed the Co from the alloy surface and the trapped subsurface Co was confirmed by CV and electron energy loss spectroscopy (EELS). RDE test of near surface Ag-Co nanoparticles in 0.1 M NaOH revealed the superior activity of this alloy for ORR compared to Ag and Ag-Co prepared by conventional slow heating process (Figure 9, B and C). The superior activity of near surface Ag-Co alloy nanoparticles was ascribed to the ligand phenomenon which involves the perturbation of the surface electronic structure by the subsurface atoms. Moreover the activity of near surface Ag-Co nanoalloy was found to be less sensitive to electrolyte contaminants compared to Pt in alkaline media. The poor stability of Pt/C in alkaline media has been recently reported. [169] AST (Accelerated stability test) performed in 0.1 M NaOH between a potential of 0.1 V and 1.23 V vs. RHE confirmed the instability of Pt/C in alkaline media. A 60% loss of the electrochemical specific area (ECSA) in alkaline media was observed compared to only 20% loss in acidic environment. Very recently Jiang *et al.* reported a bioinorganic hybrid (BIH) catalyst made from Ag-Co nanoalloy and Hemin supported on GNP (graphene Nano-platelets) for ORR in alkaline media [170]. The BIH was reported to have catalytic activity of more than ten times as compared to pure Ag and almost 80% of that of the state of the art Pt/C measured at 0.8 V vs. RHE.

Bimetallic Ag-Ni nanoalloy particles have been reported by reduction of salts.[171] Ag-Ni particles were synthesized in different atomic ratios. The Ag_3Ni composition was found to be the most active for ORR in 0.1 M NaOH. Core shell structure was proposed on basis of XRD and HRTEM which was further validated by the cyclic voltammetry. Further heat treatment at 500 ^oC was found to improve the degree of alloying of the Ag_3Ni nanoalloy. The heat treated nanoalloy was observed to have a 2.5 times higher activity compared to the Ag/C. Ag-Mn alloy nanowires have been deposited on CNT by electroless deposition method. Absence of elemental Mn in XRD data along with decrease in lattice parameter confirmed alloying of Mn with Ag in nanowires. However the Ag-Mn/CNT had a similar onset potential and lower current density values compared to Ag/CNT nanowires implying no enhancement in the catalytic activity by Mn addition. [172]

View Article Online
DOI: 10.1039/C5CY02270C

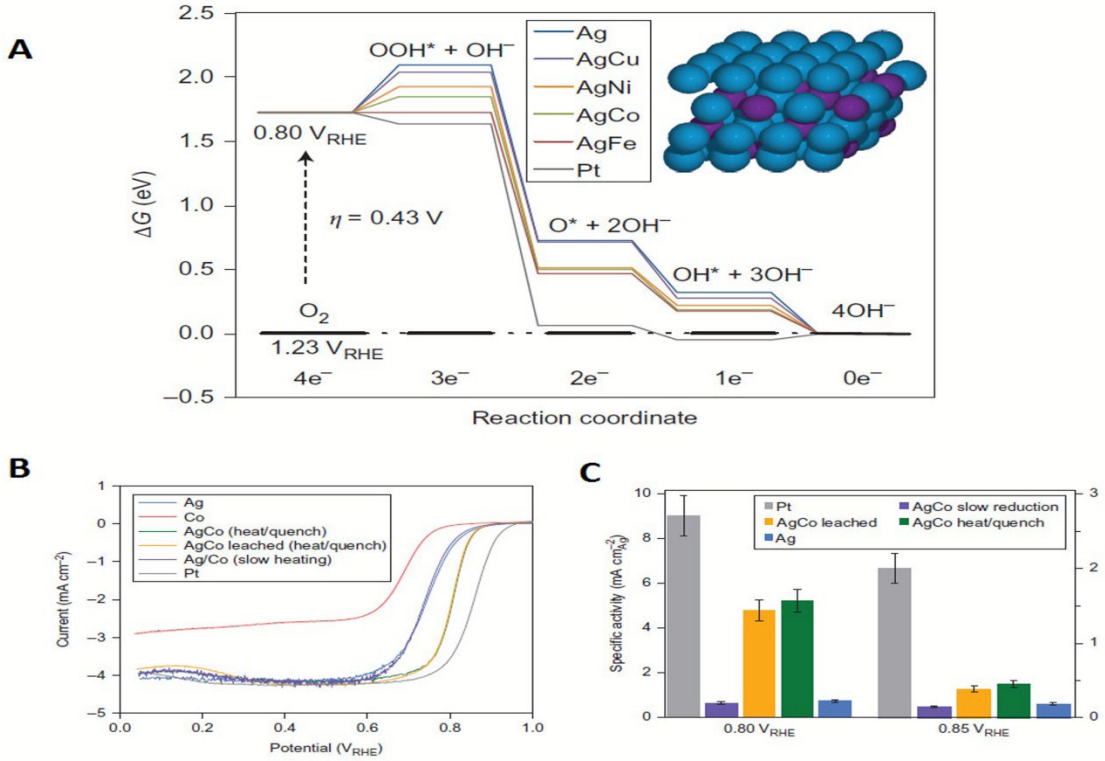

Figure 9 Computational and Experimental performance of Ag-Co nanoalloy. (A) DFT-calculated free-energy diagram for ORR on alloy catalyst surfaces. (B) Rotating disk electrode polarization curves taken in O2-saturated 0.1M NaOH at 25 °C and 900 revolutions per minute for the Ag–Co surface alloy, as well as a leached alloy, segregated Ag/Co sample and pure Ag and Co. (C) specific activities at 0.8V, 0.85V vs. V_{RHE} respectively. Adapted with permission from ref. 103. Copyright 2014 Nature Publishing Group.

3.5 Ag-M(M=Mg, Sn) alloys

The main group metals Mg and Sn are major alloying elements in bulk silver alloy. Alloying of Mg with silver has been reported to improve the ORR activity. [173, 174] Porous electrodes of Ag-Mg alloys in atomic ratios of 1:1, 1:3 and 3:1 were synthesized. Alloy with Ag:Mg ratio of 3:1 showed the highest current density i.e. 240 mA at an overpotential of 300 mV. Nanoporous Ag-Sn film has been recently reported as being active for both ORR and oxygen evolution reaction (OER). [175] The nanoporous structure was developed by the anodization of Ag-Sn alloy deposited onto a Cu film (Figure 10A). The Associated scanning electron microscope (SEM), TEM and elemental mapping is shown (Figure 10, B-D). Nanoporous Ag-Sn film was evaluated for bifunctional activity without carbon support. CV analysis revealed the superior activity of nanoporous Ag-Sn film compared to both compact Ag-Sn alloy and SnO_2. A four electron pathway was found to be dominant for ORR in 0.1 M NaOH. Ag_4Sn intermetallic nanoparticles supported on carbon were developed by ultrasonic assisted solution phase co-reduction method. [176] The Ag_4Sn particles had an average particle size of 5 nm. XPS analysis supported the formation of Ag_4Sn intermetallic with presence of surface SnO/SnO_2. RDE test showed a more positive onset potential for Ag_4Sn/C compared to Ag/C along with a much higher mass activity. The electron transfer number was close to 4 for both Ag_4Sn/C and Ag/C suggesting a dominant 4 electron transfer pathway. The authors attributed the enhanced ORR activity to the synergistic effect of Ag and Sn. Initially oxygen is chemisorbed at the SnO_x site followed by reduction at the Ag site. Moreover the Ag_4Sn/C intermetallic nanoparticles showed good methanol tolerance indicating possibility of use in direct methanol alkaline fuel cells. Similar synergistic effect has also been reported for the Ag nanocrystals deposited onto pre synthesized Cu nanowires. [177] Ag nanocrystals with an average size of

View Article Online
DOI: 10.1039/C5CY02270C

10.6 nm were deposited onto octopus tentacle shaped Cu nanowires. The resulting bimetallic structure was observed to have better ORR behavior in terms of onset potential and mass activity compared to standalone Cu nanowires or Ag nanocrystals.

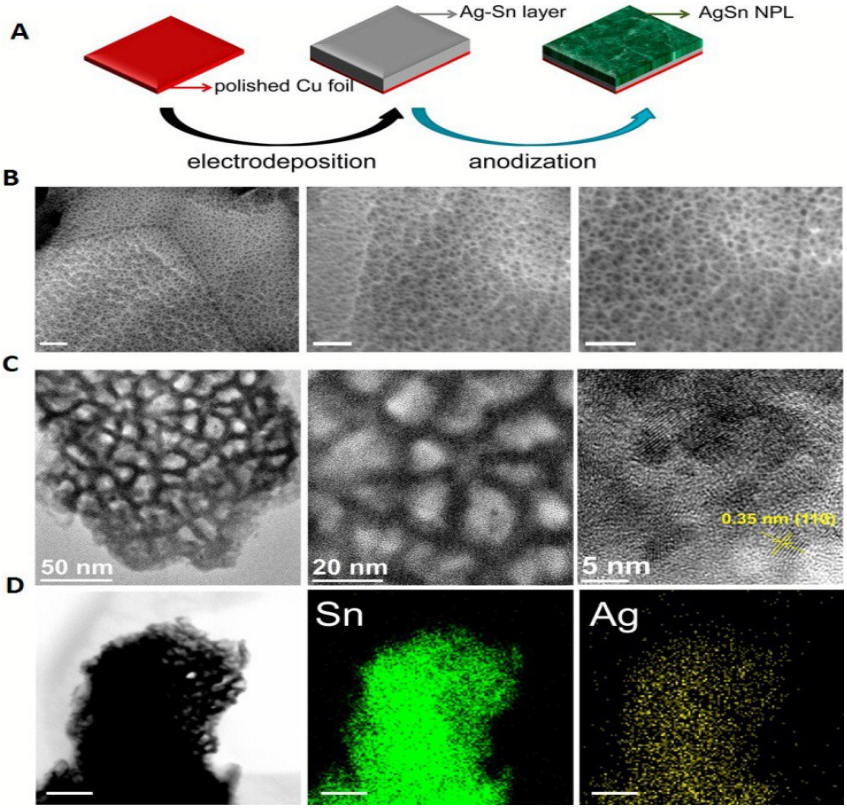

Figure 10 Nanoporous AgSn layer. (A) Schematic illustration of the fabrication processes. (B) SEM images of the AgSn nanoporous layer with different magnifications. The scale bar in b denotes 100 nm. (C) TEM images of the AgSn nanoporous layer with different magnifications. The lattice fringes, as indicated in the high-resolution TEM image (right), is ~0.35 nm and can be ascribed to SnO2 (110). (D) TEM image and elemental mapping of the AgSn nanoporous layer. The scale bar in d denotes 50 nm. Reprinted with permission from ref. 175. Copyright 2015 American Chemical Society.

3.6 Silver based multi-metallic catalysts

Multimetallic compositions in case of Pt alloys have been identified by first principle calculations to modulate the binding energy of OH on the alloy surface. [41, 42] According to the Sabatier volcano of oxygen reduction electrocatalysts, a decrease in binding energy of OH on Pt(111) by nearly 0.1 eV will maximize the catalytic activity. [102] This computational notion has been validated in case of ternary alloys of Pt where better stability along with improved catalytic activity has been achieved. [178] DFT calculations have also identified candidate Ag ternary alloy compositions for ORR. Oxygen reduction activity of core shell Ag/CuPd nanoparticles was evaluated by a combination of computational and experimental method. [179] The binding energy of oxygen E_O was used as a guideline in computational analysis. By varying shell thickness and composition, the strain in the surface of Ag/CuPd nanoparticles was varied which was used for tuning of oxygen binding energy E_O (Figure 11A). Three Ag/Cu_xPd_y Nanoparticle models were constructed with x/y = 2/7, 1/2, and 2/1, with the same core diameter of 3.2 nm (16 atomic layers) and shell thickness of 0.8 nm (4 atomic layers) (Figure 11B). The compressive strain on the NPs surface increases with the Cu concentration in the alloy (Figure 11C). From composition and strain distributions the binding energy of oxygen was measured for each model as shown by dashed boxes (Figure 11A). The ORR activity of Ag/Cu_xPd_y NPs was categorized as $Ag/CuPd_2$ > Ag/Cu_2Pd_7 > Ag/Cu_2Pd. The effect of varying shell thickness on ORR of $Ag/CuPd_2$ NPs was also investigated. Three shell thicknesses of 0.4, 0.8, and 1.2 nm were used to measure surface

View Article Online
DOI: 10.1039/C5CY02270C

strain distributions in these NPs (Figure 11, D and E). The compressive strain in the shell was observed to increase with the shell thickness by DFT calculations. The $Ag/CuPd_2$ NPs with 0.8 and 1.2 nm shell thicknesses had strain distributions which were similar and better than 0.4 nm shell for the ORR.

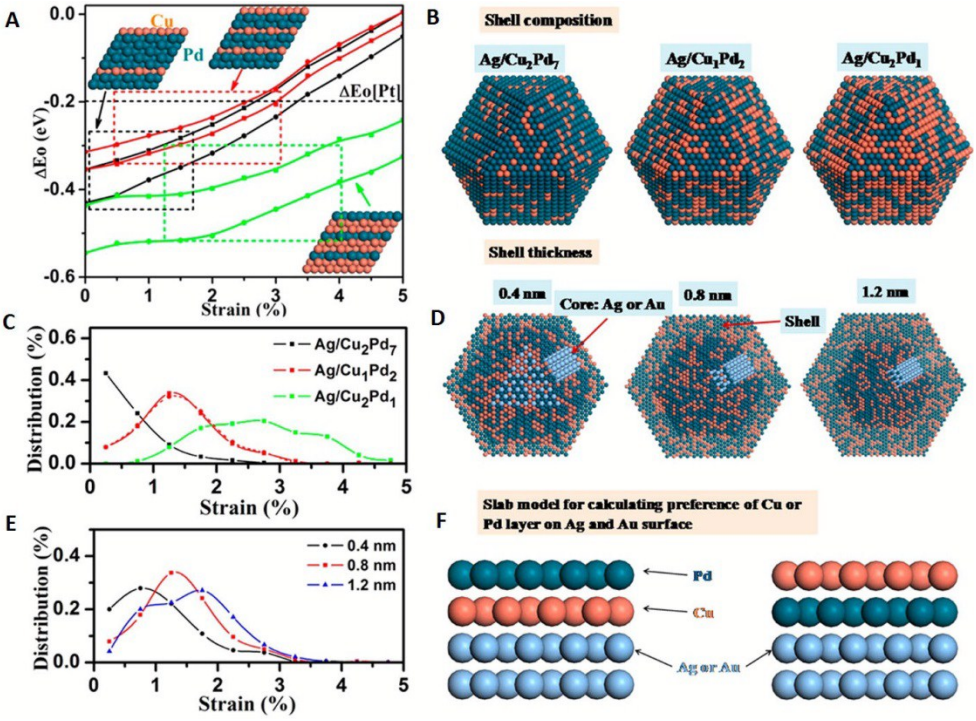

Figure 11 Computational Analysis of Ag/CuPd nanoalloy. (A) ΔE_O as a function of strain and composition. Black, red, and green curves represent Cu/Pd atomic ratios of 2/7, 1/2, and 2/1, respectively. Several curves in each color correspond to various fcc hollow sites for O adsorption. ΔE_O on the Pt(111) surface is indicated by the dashed horizontal line. Black, red, and green boxes outline the possible ΔE_O values on Ag/Cu_2Pd_7, $Ag/CuPd_2$, and Ag/Cu_2Pd NPs, respectively. (B,C) Models of core/shell NPs for various shell compositions with a shell thickness of 0.8 nm (B) and evaluated distribution of surface strain on these core/shell NPs (C). The dashed curve in (C) indicates $Au/CuPd_2$ NPs. (D, E) Models of core/shell NPs for various shell thickness with a composition of $CuPd_2$ (D) and evaluated distribution of surface strain on these core/shell NPs (E). (F) Slab models for calculation of Pd|Cu|M (left) and Cu|Pd|M (right) interfacial energies. Reprinted with permission from ref. 179. Copyright 2014 American Chemical Society.

Guided by the DFT calculations, monodisperse M/CuPd (M=Au,Ag) NPs were synthesized by co-reduction of palladium and copper precursors in the presence of 3.1 nm Ag or Au seeds with shell thicknesses of 0.4, 0.75, and 1.1 nm and compositions of $Cu_{20}Pd_{80}$, $Cu_{37}Pd_{63}$, and $Cu_{55}Pd_{45}$. Analysis of ORR on these nanocatalysts was done by RDE in 0.1 M KOH. Half-wave potentials for both $Ag/Cu_{37}Pd_{63}$ and $Au/Cu_{40}Pd_{60}$ NPs shifted towards more positive values than that of the commercial Pt/C catalyst (Figure 12A). The similar Tafel plots of $Ag/Cu_{37}Pd_{63}$ and commercial Pt implies a similar reaction mechanism for ORR on these catalyst surfaces (Figure 12B). The mass activities of the $Ag/Cu_{37}Pd_{63}$ (0.18 A/mg of Pd) and $Au/Cu_{40}Pd_{60}$ (0.20 A/mg of Au+Pd) are about three times greater than that of the commercial Pt catalyst i.e. 0.06 A/mg of Pt under the same detection conditions (Figure 12C). The durability of the Ag/CuPd NPs and Pt was evaluated at −0.30 V (a potential located at the mixed kinetic region) by a 48000s i−t test (Figure 12D). The Ag/CuPd catalyst revealed 77.6% retention of current density compared to 62.9% retention of the Pt catalyst, demonstrating the long term stability of Ag/CuPd over Pt. Palladium silver nickel Pd_2NiAg nanocrystals having a fivefold twinned structure and activity better than the 20% Pt/C have also been reported [180]. The high activity of these 15 nm size nanocrystals was attributed to the modification of surface by the Ni atoms. This lead to an optimum binding strength of oxygen intermediates for the Pd_2NiAg nanocrystals confirmed by DFT calculations. The stability of fivefold twinned Pd_2NiAg nanocatalyst was superior to 20% Pt/C in alkaline media. Twinned nanoparticles AgPd@Pt with catalytic activity at par with the commercial Pt/C catalysts have

View Article Online
DOI: 10.1039/C5CY02270C

been previously reported. [181] Presence of Ag in the core of these multimetallic core-shell nanoparticles was identified as vital for the development of twinned structure. On the other hand Pd presence in the core along with Ag reduced the tensile strain effect of Ag on surface Pt. This atomistic arrangement of atoms of multiple twinned $AgPd_{core}Pt_{shell}$ nanoparticles provided the optimum binding for ORR intermediates.

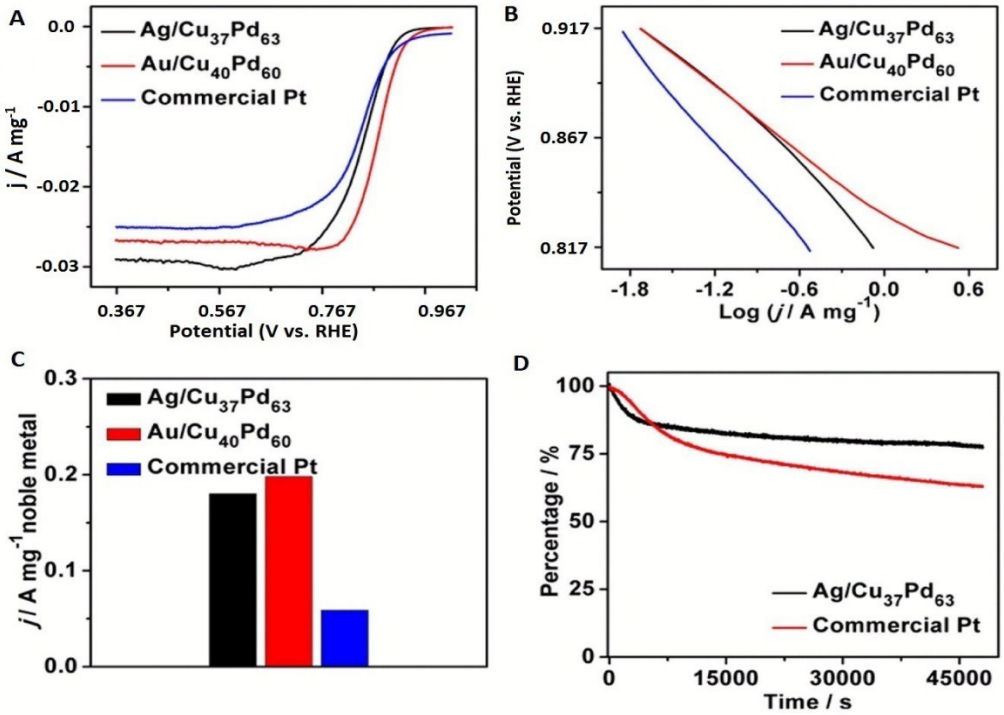

Figure 12 Electrocatalytic performance of trimetallic nanoalloy. (A) ORR polarization curves. (B) Tafel plots (C) ORR mass activity summaries at 0.867 V of $Ag/Cu_{37}Pd_{63}$, $Au/Cu_{40}Pd_{60}$, and commercial Pt in O_2-saturated 0.1 M KOH solution at 293 K. Scan rate: 10 mV/s. Rotation rate: 400 rpm. (D) Chronoamperometric responses for the ORR on $Ag/Cu_{37}Pd_{63}$ NPs and commercial Pt at 0.667 V. Rotation rate: 200 rpm. Adapted with permission from ref. 179. Copyright 2014 American Chemical Society.

A summary of electrocatalytic properties of some silver nanoalloys along with corresponding values of commercial 20% Pt/C, Ag bulk, Ag nanoparticles and highly active Ag based composites are mentioned in Table 2. Of all the silver nanoalloy systems, Ag-Pd nanoalloys have been reported to have the highest amount of catalytic activity in the potential window of 0.8-0.9 V vs. RHE. This coupled with their well-established methanol/ethanol tolerance, makes them a prime candidate for direct alcohol fuel cell applications where fuel cross over is an important design consideration. Moreover some of the Ag-Pd systems have mass and specific activity values superior to the commercial 20% Pt/C. [142, 144] This combination of activity and stability in the practical potential and environmental conditions makes them a realistic option for replacement of more costly and less stable Pt in alkaline electrolytes. Ag-Au system has been reported with reasonable onset potential and half wave potential than the constituent pure metals but the mass activity & specific activity of these nanoalloys have yet to be compared with commercial 20% Pt/C in the potential window of interest. Ag-Co nanoalloys have recently gained much interest because of 5-10 times superior activity compared to pure Ag in alkaline media. [103, 170] Near surface Ag-Co alloy has been observed to have area specific activity almost half of commercial 20% Pt/C with high stability and less sensitivity to electrolyte contaminants.[103] Incorporation of Ag-Co nanoalloy in BIH has further enhanced the activity of the hybrid catalyst to almost 80% of commercial Pt/C. [170] Ag-Cu nanoalloy catalysts deposited onto Ni-foam have attained attention recently for Zn-air rechargeable batteries because of their bifunctional working as both ORR and OER catalyst. [130] Their superior activity compared to pure Ag (more than 2.5 times) along with carbon dioxide tolerance makes

View Article Online
DOI: 10.1039/C5CY02270C

them an attractive choice for Zn air batteries. [134] The successful deposition of Ag-Cu nanoalloys onto nickel foams has been reported by PLD as well as chemical synthesis routes. This has aided in the development of carbon free supports which are not prone to corrosion and degradation at highly oxidative potentials.

Table 2 Electrocatalytic characteristics of silver nanocatalyst for ORR in alkaline electrolytes.

Catalyst	Electrolyte	Transferred Electron Number	Onset Potential (V vs. RHE)	Ref.
Ag NPs Film	0.1 M NaOH	3.7	0.86	85
Ag Polycrystalline	0.1 M NaOH	3.2	0.86	85
Ag-Cu nanoalloy	0.1 M KOH	3.7, 4	0.81, 0.9	130, 131
Ag-Cu nanoplatelets	0.1 M KOH	3.9	0.86	134
Ag_9Pd/Vulcan XC-72	0.1 M KOH	4	0.87	144
Ag/CuPd NPs	0.1 M KOH	4	c.a 0.94	179
Ag@Pd/C	1 M KOH	3.81	0.82	143
Ag@Pd/MWNT	1 M KOH	2.87	0.83	143
AgPd Nanoprisms	0.1 M KOH	3.84	c.a 0.88	147
AgCo (1:3)	1 M KOH	3	0.87	165
AgCo	0.1 M NaOH	4.03	c.a. 0.9V	103
AgCo hybrid	0.1 M KOH	4	c.a. 0.9V	170
Ag_3Ni	0.1 M NaOH	--	0.86	171
Pd_2NiAg nanocrystals	0.1 M KOH	c.a4	0.91	180
AgAu janus alloy	0.1 M NaOH	3.36	0.92	155
AgAu alloy	0.1 M NaOH	3.8-4.0	0.92	157
Ag_4Sn	0.1 M KOH	3.9	0.77	176
AgMn	0.1 M KOH	--	0.88	172
$Ag/Mn_3O_4/C$	0.1 M KOH	3.98	0.92	98
$Ag\text{-}MnO_x/C$	0.1 M KOH	3.5	0.93	117
Ag-Mo-22	1 M KOH	3.3	c.a 0.87	182
$Ag\text{-}W_2C/C$	1 M KOH	3.9	0.95	73
20% Pt/C	0.1 M NaOH	4	1.05	22

- All potentials are reported (V vs. RHE) by making appropriate conversions.

View Article Online
DOI: 10.1039/C5CY02270C

4 Challenges and future outlook.

Understanding the activity origin of silver nanoalloy is still a bottleneck for the realization of highly efficient electrocatalytic ORR in alkaline fuel cells and metal-air batteries. Continuous improvement of catalytic activity and stability of silver nanoalloys will be crucial to make the commercialization of these systems economically viable.

(1) The ORR mechanism on the surface of the nanoalloy still remains elusive. The understanding of the effect of compositional and structural variations of nanoalloy on the ORR process is crucial for the design of highly active electrocatalysts. First principle simulations along with in situ impedance spectroscopy will play an important role in the comprehension of ORR mechanism. DFT based free energy diagrams have identified the rate limiting step during ORR on a catalyst surface. [103, 125] Depending upon the formulation of the nanoalloy electrocatalyst; ligand, geometric and ensemble effect regulate the ORR activity of the catalyst. A holistic approach incorporating first principle simulations & experimental techniques is pivotal for the identification of the dominant effect of the three.

(2) The identification of the catalytically active sites during ORR on the surface of electrocatalyst is a key design consideration. Very recently Coordination-Activity plots concept has been reported for oxygen reduction in Pt based system. The active sites for ORR were found to be related to the geometric structure of the catalyst. Catalyst sites with the same number of (111) terraces but a higher number of second nearest neighbors were found to be most active towards ORR. [183] Depending upon the system, active sites for ORR can vary. For realization of highly active electrocatalyst systems it will be necessary to maximize the number of these catalytically active sites on the surface.

(3) Morphology is another important factor affecting the ORR activity. 1 dimensional nanorods and nanoporous system have been reported with high activity for ORR in alkaline media. Especially for the Ag based systems in which the weak adsorption of the ORR intermediates is the reason for low activity, these high surface energy sites increase the adsorption of intermediated resulting in faster ORR kinetics. The core shell morphology is of great prospect in this regards for both the binary and ternary silver nanoalloys. The adsorption strength of oxygen ORR intermediates on the shell surface can be tuned by the underlying core. In case of bi-metallic shell A-B, O=O bond scission can take place at an A-site followed by electro-reduction at site B on the shell

(4) Composites/ Hybrids based on silver nanoalloys hold the possibility of superior catalytic activity and stability compared to commercial Pt/C. This has been true in case of Ag-Mn_3O_4/C where covalent interactions because of proximity of Ag-Mn_3O_4 lead to improved catalytic activity. [115] In the case of manganese oxide and tungsten carbide composites with Ag, catalytic activity equal to commercial Pt/C has been reported. [73, 98, 116] Apart from high activity compared to Pt/C, these composites can offer superior alcohol tolerance which will be of great significance for the direct alcohol fuel cells. Silver nanoalloy composites with metal oxide (Mn_xO_y , Co_3O_4) can offer bifunctional ORR and OER catalytic activity, where Ag nanoalloy dominates in ORR while the metal oxide plays the pivotal role for OER. These silver nanoalloy composites can be employed in rechargeable metal-air batteries where bifunctional catalyst activity is of utmost significance. The use of bifunctional electrocatalyst would aid in reducing the charge-discharge overpotential thereby increasing the efficiency of the rechargeable battery.

(5) The ORR process takes place at the heart of the cathode where three phase boundary is present. Good access of oxygen from air, ions from the electrolyte and electrons from the

View Article Online
DOI: 10.1039/C5CY02270C

support is pivotal for the smooth and stable ORR kinetics. Binder free and carbon free deposition of electrocatalysts onto porous cathodic structures like nickel foam will become more popular for bifunctional catalysts because of larger availability of three phase boundary regions along with higher stability during charge/discharge cycle. [175] A catalyst with high activity would perform poorly in the battery if sufficient three phase regions are not provided in cathode structure. So, apart from highly active cathode catalyst, a good structural design of cathode is also an important design consideration.

Acknowledgments: This study was supported by the National Natural Science Foundation of China (grant nos. 51271148 and 50971100), the Aeronautic Science Foundation Program of China (grant no. 2012ZF53073), the Science and Technology Innovation Fund of Western Metal Materials (grant no. XBCL-2-11) and the Doctoral Fund of Ministry of Education of China (grant no. 20136102110013).

References.

1. C. McGlade and P. Ekins, *Nature*, 2015, 517, 187-190.
2. H. D. Matthews and K. Caldeira, *Geophysical Research Letters*, 2008, 35, L04705.
3. O. Erdinc and M. Uzunoglu, *Renew Sust Energ Rev*, 2012, 16, 1412-1425.
4. T. Okazaki, Y. Shirai and T. Nakamura, *Renewable Energy*, 2015, 83, 332-338.
5. J. S. Lee, S. T. Kim, R. Cao, N. S. Choi, M. Liu, K. T. Lee and J. Cho, *Advanced Energy Materials*, 2011, 1, 34-50.
6. M. A. Rahman, X. J. Wang and C. Wen, *Journal of Applied Electrochemistry*, 2014, 44, 5-22.
7. X. W. Zhang, S. H. Chan, H. K. Ho, S. C. Tan, M. Y. Li, G. J. Li, J. Li and Z. P. Feng, *International Journal of Hydrogen Energy*, 2015, 40, 6866-6919.
8. G. J. Offer, D. Howey, M. Contestabile, R. Clague and N. P. Brandon, *Energy Policy*, 2010, 38, 24-29.
9. N. Garcia-Araez and P. Novak, *J Solid State Electr*, 2013, 17, 1793-1807.
10. M. L. Perry and T. F. Fuller, *Journal of the Electrochemical Society*, 2002, 149, S59-S67.
11. A. Tewari, V. Sambhy, M. U. Macdonald and A. Sen, *Journal of Power Sources*, 2006, 153, 1-10.
12. Y. Zhao, H. M. Yu, F. Xie, Y. X. Liu, Z. G. Shao and B. L. Yi, *Journal of Power Sources*, 2014, 269, 1-6.
13. J. L. Wang, L. L. Wang, R. J. Feng and Y. Zhang, *Solid State Ionics*, 2015, 278, 144-151.
14. L. A. Adams, S. D. Poynton, C. Tamain, R. C. T. Slade and J. R. Varcoe, *Chemsuschem*, 2008, 1, 79-81.
15. in *US Department of Energy*.
16. M. K. Debe, *Nature*, 2012, 486, 43-51.
17. M. Pourbaix, *Atlas of electrochemical equilibria in aqueous solutions*, National Association of Corrosion Engineers, Houston, Tex., 2d English edn., 1974.
18. J. R. Varcoe, R. C. T. Slade, G. L. Wright and Y. L. Chen, *Journal of Physical Chemistry B*, 2006, 110, 21041-21049.
19. A. Wieckowski and J. Spendelow, in *Encyclopedia of Applied Electrochemistry*, eds. G. Kreysa, K. Ota and R. Savinell, Springer New York, 2014, DOI: 10.1007/978-1-4419-6996-5_482, ch. 482, pp. 1491-1496.
20. L. Xin, Z. Zhang, Z. Wang, J. Qi and W. Li, *Frontiers in Chemistry*, 2013, 1, 16.
21. J. J. Han, N. Li and T. Y. Zhang, *Journal of Power Sources*, 2009, 193, 885-889.
22. L. Demarconnay, C. Coutanceau and J. M. Leger, *Electrochimica Acta*, 2004, 49, 4513-4521.

View Article Online
DOI: 10.1039/C5CY02270C

23. Y. Zhou, Q. Lu, Z. B. Zhuang, G. S. Hutchings, S. Kattel, Y. S. Yan, J. G. G. Chen, J. Q. Xiao and F. Jiao, *Advanced Energy Materials*, 2015, 5, 1500149.
24. E. Morallon, J. L. Vazquez and A. Aldaz, *Journal of Electroanalytical Chemistry*, 1992, 334, 323-338.
25. N. Ramaswamy and S. Mukerjee, *Advances in Physical Chemistry*, 2012, 2012, 491604.
26. Y. W. Yihu Dai, Bin Liu & Yanhui Yang, *Small* 2014, 11, 268-289.
27. O. G. Ellert, M. V. Tsodikov, S. A. Nikolaev and V. M. Novotortsev, *Russian Chemical Reviews*, 2014, 83, 718.
28. L. Piccolo, in *Nanoalloys*, eds. D. Alloyeau, C. Mottet and C. Ricolleau, Springer London, 2012, DOI: 10.1007/978-1-4471-4014-6_11, ch. 11, pp. 369-404.
29. R. Loukrakpam, S. Y. Shan, V. Petkov, L. F. Yang, J. Luo and C. J. Zhong, *J Phys Chem C*, 2013, 117, 20715-20721.
30. Y. J. Kang, J. Snyder, M. F. Chi, D. G. Li, K. L. More, N. M. Markovic and V. R. Stamenkovic, *Nano Letters*, 2014, 14, 6361-6367.
31. M. K. Debe, A. K. Schmoeckel, G. D. Vernstrorn and R. Atanasoski, *Journal of Power Sources*, 2006, 161, 1002-1011.
32. J. K. Norskov, J. Rossmeisl, A. Logadottir, L. Lindqvist, J. R. Kitchin, T. Bligaard and H. Jonsson, *Journal of Physical Chemistry B*, 2004, 108, 17886-17892.
33. J. Greeley and J. K. Norskov, *J Phys Chem C*, 2009, 113, 4932-4939.
34. H. A. Hansen, J. Rossmeisl and J. K. Norskov, *Physical Chemistry Chemical Physics*, 2008, 10, 3722-3730.
35. K. Shin, D. H. Kim, S. C. Yeo and H. M. Lee, *Catalysis Today*, 2012, 185, 94-98.
36. K. Shin, D. H. Kim and H. M. Lee, *Chemsuschem*, 2013, 6, 1044-1049.
37. D. C. Ford, A. U. Nilekar, Y. Xu and M. Mavrikakis, *Surface Science*, 2010, 604, 1565-1575.
38. C. X. Yang, B. Huang, L. Xiao, Z. D. Ren, Z. L. Liu, J. T. Lu and L. Zhuang, *Chemical Communications*, 2013, 49, 11023-11025.
39. X. Zhang and G. Lu, *J Phys Chem Lett*, 2014, 5, 292-297.
40. F. Calle-Vallejo, M. T. M. Koper and A. S. Bandarenka, *Chem Soc Rev*, 2013, 42, 5210-5230.
41. H. L. Xin, A. Holewinski, N. Schweitzer, E. Nikolla and S. Linic, *Topics in Catalysis*, 2012, 55, 376-390.
42. H. L. Xin, A. Holewinski and S. Linic, *Acs Catalysis*, 2012, 2, 12-16.
43. G. F. Wei, Y. H. Fang and Z. P. Liu, *J Phys Chem C*, 2012, 116, 12696-12705.
44. R. B. Rankin and J. Greeley, *Acs Catalysis*, 2012, 2, 2664-2672.
45. H. A. Hansen, V. Viswanathan and J. K. Norskov, *J Phys Chem C*, 2014, 118, 6706-6718.
46. J. S. Spendelow and A. Wieckowski, *Physical Chemistry Chemical Physics*, 2007, 9, 2654-2675.
47. A. M. Gomez-Marin, R. Rizo and J. M. Feliu, *Catalysis Science & Technology*, 2014, 4, 1685-1698.
48. D. Mei, Z. D. He, Y. L. Zheng, D. C. Jiang and Y. X. Chen, *Physical Chemistry Chemical Physics*, 2014, 16, 13762-13773.
49. R. Rizo, E. Herrero and J. M. Feliu, *Physical Chemistry Chemical Physics*, 2013, 15, 15416-15425.
50. T. J. Schmidt, V. Stamenkovic, P. N. Ross and N. M. Markovic, *Physical Chemistry Chemical Physics*, 2003, 5, 400-406.
51. A. J. Bard and L. R. Faulkner, *Electrochemical methods : fundamentals and applications*, Wiley, New York, 2nd edn., 2001.
52. T. J. Schmidt, H. A. Gasteiger, G. D. Stab, P. M. Urban, D. M. Kolb and R. J. Behm, *Journal of the Electrochemical Society*, 1998, 145, 2354-2358.
53. S. Treimer, A. Tang and D. C. Johnson, *Electroanalysis*, 2002, 14, 165-171.

View Article Online
DOI: 10.1039/C5CY02270C

54. K. J. J. Mayrhofer, D. Strmcnik, B. B. Blizanac, V. Stamenkovic, M. Arenz and N. M. Markovic, *Electrochimica Acta*, 2008, 53, 3181-3188.
55. F. Si, Y. Zhang, L. Yan, J. Zhu, M. Xiao, C. Liu, W. Xing and J. Zhang, in *Rotating Electrode Methods and Oxygen Reduction Electrocatalysts*, ed. W. X. Y. Zhang, Elsevier, Amsterdam, 2014, DOI: http://dx.doi.org/10.1016/B978-0-444-63278-4.00004-5, pp. 133-170.
56. D. Sepa, M. Vojnovic and Damjanov.A, *Electrochimica Acta*, 1970, 15, 1355-1366.
57. D. B. Sepa, M. V. Vojnovic and A. Damjanovic, *Electrochimica Acta*, 1980, 25, 1491-1496.
58. H. H. Yang and R. L. McCreery, *Journal of The Electrochemical Society*, 2000, 147, 3420-3428.
59. N. D. Merkulova, B. N. Efremov, G. V. Zhutaeva, N. A. Shumilova and V. S. Bagotskii, *Sov Electrochem+*, 1975, 11, 758-761.
60. I. A. Kukushkina, G. V. Shteinberg and V. S. Bagotskii, *Sov Electrochem+*, 1975, 11, 1060-1063.
61. B. B. Blizanac, P. N. Ross and N. M. Markovic, *Electrochimica Acta*, 2007, 52, 2264-2271.
62. S. M. Park, S. Ho, S. Aruliah, M. F. Weber, C. A. Ward, R. D. Venter and S. Srinivasan, *Journal of The Electrochemical Society*, 1986, 133, 1641-1649.
63. C. F. Zinola, A. M. C. Luna and A. J. Arvia, *Electrochimica Acta*, 1994, 39, 1951-1959.
64. N. Alexeyeva, K. Tammeveski, A. Lopez-Cudero, J. Solla-Gullon and J. M. Feliu, *Electrochimica Acta*, 2010, 55, 794-803.
65. L. Genies, Y. Bultel, R. Faure and R. Durand, *Electrochimica Acta*, 2003, 48, 3879-3890.
66. D. B. Sepa, M. V. Vojnovic, L. M. Vracar and A. Damjanovic, *Electrochimica Acta*, 1987, 32, 129-134.
67. D. B. Sepa, M. V. Vojnovic and A. Damjanovic, *Electrochimica Acta*, 1981, 26, 781-793.
68. Damjanov.A and V. Brusic, *Electrochimica Acta*, 1967, 12, 615-628.
69. A. B. Anderson, *Electrochimica Acta*, 2002, 47, 3759-3763.
70. N. A. Anastasijević, V. Vesović and R. R. Adžić, *Journal of Electroanalytical Chemistry and Interfacial Electrochemistry*, 1987, 229, 305-316.
71. B. B. Blizanac, P. N. Ross and N. M. Markovic, *Journal of Physical Chemistry B*, 2006, 110, 4735-4741.
72. F. P. Hu, X. G. Zhang, F. Xiao and J. L. Zhang, *Carbon*, 2005, 43, 2931-2936.
73. H. Meng and P. K. Shen, *Electrochemistry Communications*, 2006, 8, 588-594.
74. C. C. M. Neumann, E. Laborda, K. Tschulik, K. R. Ward and R. G. Compton, *Nano Research*, 2013, 6, 511-524.
75. M. Chatenet, L. Genies-Bultel, M. Aurousseau, R. Durand and F. Andolfatto, *Journal of Applied Electrochemistry*, 2002, 32, 1131-1140.
76. E. R. Yeager, M.; Gervasio, D.; Razaq, A.; Tryk, D, presented in part at the Proceedings of the Workshop on Structural Effects in Electrocatalysis and Oxygen Electrochemistry The Electrochemical Society, Pennington NJ, 1992.
77. N. M. Markovic, H. A. Gasteiger and N. Philip, *J Phys Chem-Us*, 1996, 100, 6715-6721.
78. Q. Y. Wang, X. Q. Cui, W. M. Guan, L. Zhang, X. F. Fan, Z. Shi and W. T. Zheng, *Journal of Power Sources*, 2014, 269, 152-157.
79. S. Strbac, *Electrochimica Acta*, 2011, 56, 1597-1604.
80. L. Genies, R. Faure and R. Durand, *Electrochimica Acta*, 1998, 44, 1317-1327.
81. N. Ramaswamy and S. Mukerjee, *J Phys Chem C*, 2011, 115, 18015-18026.
82. R. Li, H. B. Li, S. L. Xua and J. F. Liu, *Applied Surface Science*, 2015, 351, 853-861.
83. A. J. Bard, *J Am Chem Soc*, 2010, 132, 7559-7567.
84. Z. C. Wang, L. Xin, X. S. Zhao, Y. Qiu, Z. Y. Zhang, O. A. Baturina and W. Z. Li, *Renewable Energy*, 2014, 62, 556-562.
85. P. Singh and D. A. Buttry, *J Phys Chem C*, 2012, 116, 10656-10663.
86. Y. Z. Lu and W. Chen, *Journal of Power Sources*, 2012, 197, 107-110.

View Article Online
DOI: 10.1039/C5CY02270C

87. J. Ohyama, Y. Okata, N. Watabe, M. Katagiri, A. Nakamura, H. Arikawa, K. Shimizu, T. Takeguchi, W. Ueda and A. Satsuma, *Journal of Power Sources*, 2014, 245, 998-1004.
88. N. Wang, X. Cao, Q. J. Chen and G. Lin, *Chem-Eur J*, 2012, 18, 6049-6054.
89. C. L. Lee and C. C. Syu, *International Journal of Hydrogen Energy*, 2011, 36, 15068-15074.
90. Y. Z. Lu, Y. C. Wang and W. Chen, *Journal of Power Sources*, 2011, 196, 3033-3038.
91. M. A. Kostowskyj, R. J. Gilliam, D. W. Kirk and S. J. Thorpe, *International Journal of Hydrogen Energy*, 2008, 33, 5773-5778.
92. S. Mukerjee, S. Srinivasan, M. P. Soriaga and J. Mcbreen, *Journal of the Electrochemical Society*, 1995, 142, 1409-1422.
93. B. Hammer and J. K. Norskov, *Adv Catal*, 2000, 45, 71-129.
94. V. R. Stamenkovic, B. S. Mun, K. J. J. Mayrhofer, P. N. Ross and N. M. Markovic, *J Am Chem Soc*, 2006, 128, 8813-8819.
95. X. H. Tan, S. Prabhudev, A. Kohandehghan, D. Karpuzov, G. A. Botton and D. Mitlin, *Acs Catalysis*, 2015, 5, 1513-1524.
96. Y. Xu, A. V. Ruban and M. Mavrikakis, *J Am Chem Soc*, 2004, 126, 4717-4725.
97. G. W. Wang, B. Huang, L. Xiao, Z. D. Ren, H. Chen, D. L. Wang, H. D. Abruna, J. T. Lu and L. Zhuang, *J Am Chem Soc*, 2014, 136, 9643-9649.
98. S. A. Park, H. Lim and Y. T. Kim, *Acs Catalysis*, 2015, 5, 3995-4002.
99. V. R. Stamenkovic, B. S. Mun, M. Arenz, K. J. J. Mayrhofer, C. A. Lucas, G. F. Wang, P. N. Ross and N. M. Markovic, *Nature Materials*, 2007, 6, 241-247.
100. M. H. Seo, S. M. Choi, J. K. Seo, S. H. Noh, W. B. Kim and B. Han, *Appl Catal B-Environ*, 2013, 129, 163-171.
101. F. H. B. Lima, J. Zhang, M. H. Shao, K. Sasaki, M. B. Vukmirovic, E. A. Ticianelli and R. R. Adzic, *The Journal of Physical Chemistry C*, 2007, 111, 404-410.
102. I. E. L. Stephens, A. S. Bondarenko, F. J. Perez-Alonso, F. Calle-Vallejo, L. Bech, T. P. Johansson, A. K. Jepsen, R. Frydendal, B. P. Knudsen, J. Rossmeisl and I. Chorkendorff, *J Am Chem Soc*, 2011, 133, 5485-5491.
103. A. Holewinski, J. C. Idrobo and S. Linic, *Nature Chemistry*, 2014, 6, 828-834.
104. P. Strasser, S. Koh, T. Anniyev, J. Greeley, K. More, C. F. Yu, Z. C. Liu, S. Kaya, D. Nordlund, H. Ogasawara, M. F. Toney and A. Nilsson, *Nature Chemistry*, 2010, 2, 454-460.
105. K. Mohanraju and L. Cindrella, *Rsc Advances*, 2014, 4, 11939-11947.
106. J. H. Kim, S. Chang and Y. T. Kim, *Appl Catal B-Environ*, 2014, 158, 112-118.
107. J. R. Kitchin, J. K. Norskov, M. A. Barteau and J. G. Chen, *J Chem Phys*, 2004, 120, 10240-10246.
108. W. J. Tang and G. Henkelman, *J Chem Phys*, 2009, 130, 194504.
109. J. L. Fernandez, D. A. Walsh and A. J. Bard, *J Am Chem Soc*, 2005, 127, 357-365.
110. N. M. Rodriguez, A. Chambers and R. T. K. Baker, *Langmuir*, 1995, 11, 3862-3866.
111. F. Bidault, D. J. L. Brett, P. H. Middleton and N. P. Brandon, *Journal of Power Sources*, 2009, 187, 39-48.
112. M. Maja, C. Orecchia, M. Strano, P. Tosco and M. Vanni, *Electrochimica Acta*, 2000, 46, 423-432.
113. H. Matsushima, W. Majima and Y. Fukunaka, *Electrochimica Acta*, 2013, 114, 509-513.
114. L. Z. Yuan, L. H. Jiang, J. Liu, Z. X. Xia, S. L. Wang and G. Q. Sun, *Electrochimica Acta*, 2014, 135, 168-174.
115. J. J. Liu, J. Z. Liu, W. W. Song, F. Wang and Y. Song, *Journal of Materials Chemistry A*, 2014, 2, 17477-17488.
116. Q. E. Tang, L. H. Jiang, J. Qi, Q. Jiang, S. L. Wang and G. Q. Sun, *Appl Catal B-Environ*, 2011, 104, 337-345.

View Article Online
DOI: 10.1039/C5CY02270C

117. D. A. Slanac, A. Lie, J. A. Paulson, K. J. Stevenson and K. P. Johnston, *J Phys Chem C*, 2012, 116, 11032-11039.
118. S. W. Liu and X. Qin, *Rsc Advances*, 2015, 5, 15627-15633.
119. Y. Wang, X. J. Lu, Y. Liu and Y. Q. Deng, *Electrochemistry Communications*, 2013, 31, 108-111.
120. M. Cazayous, C. Langlois, T. Oikawa, C. Ricolleau and A. Sacuto, *Physical Review B*, 2006, 73, 113402.
121. S. Nunez and R. L. Johnston, *J Phys Chem C*, 2010, 114, 13255-13266.
122. W. Y. Li and F. Y. Chen, *Chinese Phys B*, 2014, 23, 117103.
123. L. Vitos, A. V. Ruban, H. L. Skriver and J. Kollar, *Surface Science*, 1998, 411, 186-202.
124. W. Q. Ma, F. Y. Chen, N. Zhang and X. Q. Wu, *Journal of Molecular Modeling*, 2014, 20, 2454.
125. N. Zhang, F. Y. Chen and X. Q. Wu, *Scientific Reports*, 2015, 5, 11984.
126. R. Ferrando, A. Fortunelli and G. Rossi, *Physical Review B*, 2005, 72, 085449.
127. G. Rossi, A. Rapallo, C. Mottet, A. Fortunelli, F. Baletto and R. Ferrando, *Phys Rev Lett*, 2004, 93, 105503.
128. R. A. Vansanten and M. Neurock, *Catal Rev*, 1995, 37, 557-698.
129. Y. M. Lei, F. Y. Chen, Y. C. Jin and Z. W. Liu, *Nanoscale Research Letters*, 2015, 10, 197.
130. X. Q. Wu, F. Y. Chen, Y. C. Jin, N. Zhang and R. L. Johnston, *Acs Appl Mater Inter*, 2015, 7, 17782-17791.
131. X. Wu, F. Chen, N. Zhang, A. Qaseem and R. L. Johnston, *Journal of Materials Chemistry A*, 2016, 4, 3527-3537.
132. Y. C. Jin and F. Y. Chen, *Electrochimica Acta*, 2015, 158, 437-445.
133. Y. G. Li, M. Gong, Y. Y. Liang, J. Feng, J. E. Kim, H. L. Wang, G. S. Hong, B. Zhang and H. J. Dai, *Nature Communications*, 2013, 4, 1805.
134. Y. C. Jin, F. Y. Chen, Y. M. Lei and X. Q. Wu, *Chemcatchem*, 2015, 7, 2377-2383.
135. J. F. Drillet, F. Holzer, T. Kallis, S. Muller and V. M. Schmidt, *Physical Chemistry Chemical Physics*, 2001, 3, 368-371.
136. H.-H. Cheng and C.-S. Tan, *Journal of Power Sources*, 2006, 162, 1431-1436.
137. A. J. Appleby and a. F. R. Foulkes, *Fuel Cell Handbook*, Krieger Publishing Company Melbourne, FL, United States, 1993.
138. E. Gülzow, *Journal of Power Sources*, 1996, 61, 99-104.
139. I. Karakaya and W. T. Thompson, *Bulletin of Alloy Phase Diagrams*, 1988, 9, 237-243.
140. P. Mulvaney, *Langmuir*, 1996, 12, 788-800.
141. C. F. Calver, P. Dash and R. W. J. Scott, *Chemcatchem*, 2011, 3, 695-697.
142. L. Jiang, A. Hsu, D. Chu and R. Chen, *Electrochimica Acta*, 2010, 55, 4506-4511.
143. R. C. Sekol, X. K. Li, P. Cohen, G. Doubek, M. Carmo and A. D. Taylor, *Appl Catal B-Environ*, 2013, 138, 285-293.
144. D. A. Slanac, W. G. Hardin, K. P. Johnston and K. J. Stevenson, *J Am Chem Soc*, 2012, 134, 9812-9819.
145. A. Dhouib and H. Guesmi, *Chemical Physics Letters*, 2012, 521, 98-103.
146. M. M. Liu, Y. Z. Lu and W. Chen, *Adv Funct Mater*, 2013, 23, 1289-1296.
147. L. Xu, Z. M. Luo, Z. X. Fan, X. Zhang, C. L. Tan, H. Li, H. Zhang and C. Xue, *Nanoscale*, 2014, 6, 11738-11743.
148. C. L. Lee, H. P. Chiou, C. M. Syu, C. R. Liu, C. C. Yang and C. C. Syu, *International Journal of Hydrogen Energy*, 2011, 36, 12706-12714.
149. W. B. Luo, X. W. Gao, S. L. Chou, J. Z. Wang and H. K. Liu, *Advanced Materials*, 2015, 27, 6862-6869.
150. R. Elliott and F. Shunk, *Bulletin of Alloy Phase Diagrams*, 1980, 1, 45-47.

View Article Online
DOI: 10.1039/C5CY02270C

151. J. H. Hodak, A. Henglein, M. Giersig and G. V. Hartland, *Journal of Physical Chemistry B*, 2000, 104, 11708-11718.
152. J. P. Wilcoxon and P. P. Provencio, *J Am Chem Soc*, 2004, 126, 6402-6408.
153. J. Zhu, Y. C. Wang, L. Q. Huang and Y. M. Lu, *Physics Letters A*, 2004, 323, 455-459.
154. R. G. Sanedrin, D. G. Georganopoulou, S. Park and C. A. Mirkin, *Advanced Materials*, 2005, 17, 1027–1031.
155. Y. Song, K. Liu and S. W. Chen, *Langmuir*, 2012, 28, 17143-17152.
156. E. Bertel, P. Roos and J. Lehmann, *Physical Review B*, 1995, 52, 14384-14387.
157. P. G. Hu, Y. Song, L. M. Chen and S. W. Chen, *Nanoscale*, 2015, 7, 9627-9636.
158. A. Q. Wang, J. H. Liu, S. D. Lin, T. S. Lin and C. Y. Mou, *Journal of Catalysis*, 2005, 233, 186-197.
159. M. Singleton and P. Nash, *Journal of Phase Equilibria*, 1987, 8, 119-121.
160. I. Karakaya and W. T. Thompson, *Bulletin of Alloy Phase Diagrams*, 1986, 7, 259-263.
161. T. Van Hoof and M. Hou, *Physical Review B*, 2005, 72, 115434.
162. E. Janssens, T. Van Hoof, N. Veldeman, S. Neukermans, M. Hou and P. Lievens, *International Journal of Mass Spectrometry*, 2006, 252, 38-46.
163. H. Portales, L. Saviot, E. Duval, M. Gaudry, E. Cottancin, M. Pellarin, J. Lerme and M. Broyer, *Physical Review B*, 2002, 65, 165422.
164. R. Ferrando, A. Fortunelli and G. Rossi, *Physical Review B*, 2005, 72.
165. F. H. B. Lima, J. F. R. de Castro and E. A. Ticianelli, *Journal of Power Sources*, 2006, 161, 806-812.
166. F. Loglio, E. Lastraioli, C. Bianchini, C. Fontanesi, M. Innocenti, A. Lavacchi, F. Vizza and M. L. Foresti, *Chemsuschem*, 2011, 4, 1112-1117.
167. Q. F. Yi and L. H. Song, *Electroanalysis*, 2012, 24, 1655-1663.
168. C. Zafferoni, G. Cioncoloni, M. L. Foresti, L. Dei, E. Carretti, F. Vizza, A. Lavacchi and M. Innocenti, *Molecules*, 2015, 20, 14386-14401.
169. A. Zadick, L. Dubau, N. Sergent, G. Berthome and M. Chatenet, *Acs Catalysis*, 2015, 5, 4819-4824.
170. R. Z. Jiang, D. T. Tran, J. P. McClure and D. Chu, *Acs Appl Mater Inter*, 2015, 7, 18530-18539.
171. X. J. Song and D. M. Zhang, *Energy*, 2014, 70, 223-230.
172. M. A. Kostowskyj, D. W. Kirk and S. J. Thorpe, *International Journal of Hydrogen Energy*, 2010, 35, 5666-5672.
173. S. Z. Beer and Y. L. Sandler, *Journal of The Electrochemical Society*, 1965, 112, 1133-1136.
174. H. K. Lee, J. P. Shim, M. J. Shim, S. W. Kim and J. S. Lee, *Materials Chemistry and Physics*, 1996, 45, 238-242.
175. Y. Yang, H. L. Fei, G. D. Ruan, L. Li, G. Wang, N. D. Kim and J. M. Tour, *Acs Appl Mater Inter*, 2015, 7, 20607-20611.
176. Y. J. Lu, N. L. Zhang, L. An, X. Li and D. G. Xia, *Journal of Power Sources*, 2013, 240, 606-611.
177. M. Han, S. L. Liu, L. Y. Zhang, C. Zhang, W. W. Tu, Z. H. Dai and J. C. Bao, *Acs Appl Mater Inter*, 2012, 4, 6654-6660.
178. X. Huang, Z. Zhao, L. Cao, Y. Chen, E. Zhu, Z. Lin, M. Li, A. Yan, A. Zettl, Y. M. Wang, X. Duan, T. Mueller and Y. Huang, *Science*, 2015, 348, 1230-1234.
179. S. J. Guo, X. Zhang, W. L. Zhu, K. He, D. Su, A. Mendoza-Garcia, S. F. Ho, G. Lu and S. H. Sun, *J Am Chem Soc*, 2014, 136, 15026-15033.
180. S. L. Liu, Q. H. Zhang, Y. F. Li, M. Han, L. Gu, C. W. Nan, J. C. Bao and Z. H. Dai, *J Am Chem Soc*, 2015, 137, 2820-2823.
181. J. H. Yang, J. Yang and J. Y. Ying, *Acs Nano*, 2012, 6, 9373-9382.

View Article Online
DOI: 10.1039/C5CY02270C

182. Y. Wang, Y. Liu, X. J. Lu, Z. P. Li, H. N. Zhang, X. J. Cui, Y. Zhang, F. Shi and Y. Q. Deng, *Electrochemistry Communications*, 2012, 20, 171-174.
183. F. Calle-Vallejo, J. Tymoczko, V. Colic, Q. H. Vu, M. D. Pohl, K. Morgenstern, D. Loffreda, P. Sautet, W. Schuhmann and A. S. Bandarenka, *Science*, 2015, 350, 185-189.

View Article Online
DOI: 10.1039/C5CY02270C